Computers and Fluids 253 (2023) 105791

Contents lists available at ScienceDirect

Computers and Fluids

journal homepage: www.elsevier.com/locate/compfluid

Algebraic modifications of the k-$\tilde{\omega}$ and Spalart–Allmaras turbulence models to predict bypass and separation-induced transition

A. Crivellini [a], A. Ghidoni [b], G. Noventa [b,*]

[a] Marche Polytechnic University, Department of Industrial Engineering and Mathematical Science, via Brecce Bianche 12, 60131, Ancona, Italy
[b] University of Brescia, Department of Mechanical and Industrial Engineering, via Branze 36, 25123 Brescia, Italy

ARTICLE INFO

Keywords:
Laminar to turbulent transition
Discontinuous Galerkin
High-order solver
Transition model
RANS equations

ABSTRACT

Many reliable and robust turbulence models are nowadays available for the Reynolds-Averaged Navier–Stokes (RANS) equations to accurately simulate a wide range of engineering flows. However, turbulence models are not suited to correctly described flows with low to moderate Reynolds numbers, which are characterized by strong transitional phenomena. Therefore, numerical models able to accurately predict transitional flows are mandatory to overcome the limits of turbulence models for the efficient design of many industrial applications. The only ways to describe transition are Direct Numerical Simulation (DNS), Large Eddy Simulation (LES), and transition models, where the computational cost of DNS and LES is still too high for their routine use in industry. A modified version of the k-$\tilde{\omega}$ and Spalart–Allmaras turbulence models is here proposed to predict transition due to the bypass and separation-induced modes. The modifications are based on the γk-$\tilde{\omega}$ and the SA-BCM models and avoid complex formulations of transport equations ad-hoc defined for transition. Both the transition models are correlation-based algebraic models that rely only on local flow information and an intermittency function, which damps the turbulent production according to some transition onset requirements. The proposed transition models are implemented in a high-order discontinuous Galerkin (dG) solver and validated on benchmark cases from the ERCOFTAC suite to the Eppler 387 airfoil, with different transition mode, freestream Reynolds number and turbulent intensity, and pressure gradient.

1. Introduction

Laminar to turbulent transition is a common phenomenon in low to moderate Reynolds number flows. In addition to the freestream Reynolds number, transition is influenced by the freestream turbulent intensity, the roughness of the surface, and the pressure gradient. The four main transition mechanism are: natural, bypass, separation-induced, and wake-induced. The modeling of the transition is very difficult, due to the complex nature, and for this reason is yet a not fully resolved problem for the scientific community.

Many reliable and robust turbulence models are available for the Reynolds-Averaged Navier–Stokes (RANS) equations to accurately simulate a wide range of engineering flows [1–4], with a lack of fidelity when the flow is transitional. In fact, turbulence models are not suited to correctly describe flows with low to moderate Reynolds numbers, which are characterized by strong transitional phenomena. As a consequence, numerical models able to accurately predict transitional flows are mandatory to overcome the limits of turbulence models for the efficient design in many industrial fields, as aerospace, turbomachinery, maritime, and automotive.

The only ways to describe transitional phenomena are Direct Numerical Simulation (DNS), Large Eddy Simulation (LES), and transition models for RANS equations, where the computational cost of DNS and LES is still too high for their routine use in industry. Many transition models are available in literature, but none of these formulations seem to be comprehensive and widely used both in the scientific community and industry.

Literature classifies transition models into non-local and local models, where also the low-Reynolds version of the turbulence models can represent a solution to describe transition. The non-local models are based on correlations, which relate the momentum thickness Reynolds number to local free-stream conditions, such as turbulence intensity and pressure gradient, where several correlations have been developed for different transition mechanisms. The main drawback is due to the fact that the non-local formulation needs the information on the integral thickness of the boundary layer and of the flow at the edge of the boundary layer. While the local models are based on transport equations for turbulent or transitional variables, similarly to the turbulence models, with only local flow information. The local formulation

* Corresponding author.
E-mail address: gianmaria.noventa@unibs.it (G. Noventa).

https://doi.org/10.1016/j.compfluid.2023.105791
Received 20 June 2022; Received in revised form 15 December 2022; Accepted 9 January 2023
Available online 11 January 2023

Nomenclature

Δx_1	Length (in x-direction) of the first element from the leading edge of the computational mesh
Δy_1	Height (in y-direction) of the first element from wall of the computational mesh
δ_{ij}	Kronecker delta (–)
γ_g	ratio of gas specific heats (–)
∞	Freestream flow conditions
λ_T	Turbulent length scale (m)
μ	Dynamic viscosity (Pa s)
$\mu_T/\mu = \nu_T/\nu$	Viscosity ratio (–)
ν	Kinematic viscosity (m^2/s)
ω	Specific dissipation rate of turbulent kinetic energy (1/s)
$\Omega = \sqrt{2\Omega_{ij}\Omega_{ij}}$	Vorticity magnitude (1/s)
$\Omega_{ij} = \left(\frac{\partial u_i}{\partial x_j} - \frac{\partial u_j}{\partial x_i}\right)$	Vorticity tensor (1/s)
ρ	Density (kg/m^3)
$\tilde{\nu}$	SA's working variable (m^2/s^2)
d	Wall-distance (m)
E	Total specific energy (J/kg)
e	Internal specific energy (J/kg)
k	Turbulent kinetic energy (m^2/s^2)
k_L	Laminar kinetic energy (m^2/s^2)
k_l	Large-scale turbulent kinetic energy (m^2/s^2)
k_s	Small-scale turbulent kinetic energy (m^2/s^2)
$k_{TOT} = k + k_L$	Total kinetic energy (m^2/s^2)
LE	Leading edge flow conditions
M	Mach number (–)
n_e	Number of elements of the computational mesh
n_x	Number of elements in x-direction of the computational mesh
p	Pressure (Pa)
Pr	Molecular Prandtl number (–)
Pr_T	Turbulent Prandtl number (–)
q_i	i-component heat flux (W/m^2)
Re	Reynolds number (–)
$Re_\omega = \frac{e^{\tilde{\omega}} d^2}{\nu}$	Specific dissipation rate Reynolds number (–)
$Re_{\sqrt{k}\,d} = \frac{\sqrt{k} d}{\nu}$	Wall-distance Reynolds number (–)
$Re_\theta = \frac{Re_{d^2\Omega}}{\nu}$	Momentum thickness Reynolds number (–)
$Re_{d\,S} = \frac{S d^2}{\nu}$	Strain-rate Reynolds number (–)
$Re_{d^2\,\Omega} = \frac{\Omega d^2}{\nu}$	Vorticity Reynolds number (–)
$Re_{k\,\Omega} = \frac{k}{\nu\Omega}$	Turbulent kinetic energy Reynolds number (–)
$Re_{k\omega} = \frac{k e^{\tilde{\omega}_r}}{\nu\Omega^2}$	Turbulent quantities Reynolds number (–)
$Re_T = \frac{f_W^2 k}{\nu e^{\tilde{\omega}}}$	Effective turbulent Reynolds number (–)
$S = \sqrt{2S_{ij}S_{ij}}$	Strain-rate magnitude (1/s)
$S_{ij} = \left(\frac{\partial u_i}{\partial x_j} + \frac{\partial u_j}{\partial x_i}\right)$	Strain-rate tensor (1/s)
Tu	Turbulent intensity (–)
u_i	i-component velocity (m/s)
x_i	i-component spatial coordinate (m)

guarantees better robustness, accuracy and easiness of implementation in modern solvers, especially for High Performance Computing (HPC) and parallel simulations. These models can be divided into correlation-based models [5], and phenomenological models [6].

The transition models have been proposed for the standard Finite Volume Methods (FVMs), but the increasing required level of resolution naturally leads to consider discretization methods with a higher order of accuracy, such as discontinuous Galerkin (dG) methods. In dG methods the solution of the weak or variational form of a partial differential problem is approximated by polynomial functions over the elements, similarly to the classical continuous Finite Element Method (FEM). However, unlike continuous FEMs, dG discretizations use an approximation that is in general discontinuous at the element interfaces. The coupling of the approximate solutions between neighboring elements is weakly enforced by interface, or numerical, fluxes. An appropriate definition of the numerical fluxes guarantee the consistency and stability of the dG numerical approximation. The main drawback of this higher accuracy is the increased computational cost compared to FVMs, but the compact stencil of dG methods, involving only one element and its neighbors, makes the formulation very well suited for massively parallel computer platforms. Furthermore, the computational efficiency of dG solvers can be substantially improved by resorting to multilevel solution approaches, such as the p-multigrid algorithms [3].

A modified version of the $k-\tilde{\omega}$ [7] and Spalart–Allmaras [4] turbulence models is here proposed and implemented in a high-order accurate dG solver, called MIGALE, in order to predict transition due to the bypass and separation-induced mode. The modifications are based on the $\gamma k-\omega$ by Holman and Fürst [8,9] and Kubacki et al. [10–12], and the SA-BCM by Cakmakcioglu et al. [13,14]. Both the models are correlation-based algebraic transition models that rely on local and freestream flow information and include an intermittency function instead of an intermittency equation. The basic idea behind the models is that, instead of writing a transport equation for intermittency, an intermittency function multiplies the production terms of the formulation of the turbulence models. In particular, the turbulence production is damped until it satisfies some transition onset requirements. The choice of these transition models falls in the fact that the starting turbulence models are yet implemented and widely assessed in the MIGALE solver (see Fig. 1). For historical reasons the $k-\tilde{\omega}$ model [7] is implemented both in the compressible and incompressible solvers, while the Spalart–Allmaras model only in the incompressible solver.

The prediction capabilities of these transition models, e.g., the $\gamma k-\tilde{\omega}$ and SA-BCM models, are proved and assessed by computing the flow over the flat plates of the ERCOFTAC T3 series with zero and non-zero pressure gradients, where the T3A, T3B, T3A-, and T3C cases are investigated experimentally by Coupland [18] and the T3L cases by Coupland and Brierley [19]. These test cases are mainly characterized by bypass and separation-induced transition, with different freestream Reynolds number Re_∞ and turbulent intensity at the leading edge of the plate Tu_{LE}. Furthermore the transitional flow around an Eppler 387 airfoil with freestream turbulent intensity $Tu_\infty = 0.1\%$ and Reynolds number $Re_\infty = 200\,000$, based on the chord of the airfoil and the freestream flow quantities, and different angles of attack is considered in comparison to the experiments by McGhee et al. [20] at Langley Low-Turbulence Pressure Tunnel (LTPT). In particular, in the T3A, T3B, T3A-, and T3C cases the transition is in the bypass mode, while in the rounded leading edge flat plates, e.g., T3L cases, and in the Eppler airfoil cases the transition is in the separation-induced mode. In the former cases the separation is due to the geometry and only the reattachment has to be triggered by the model, while in the latter cases the separation is due to the pressure gradient and the models play a

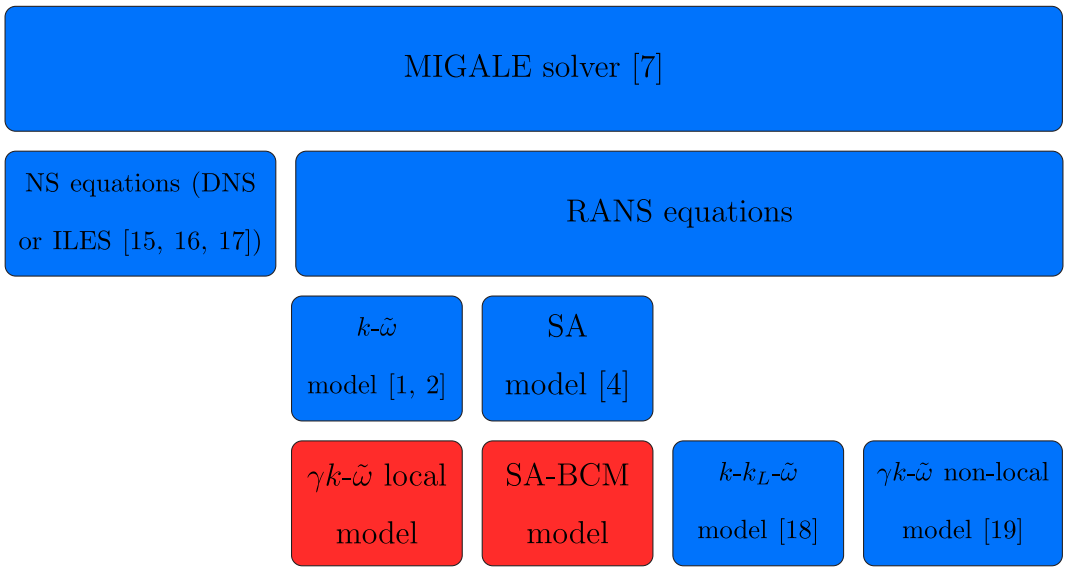

Fig. 1. Representative scheme of the MIGALE solver, where compressible and incompressible Euler, Navier–Stokes [15–17] and RANS equations are discretized and solved in a high-order spatial and temporal dG framework. The Euler equations box is neglected for a sake of clarity. Below the RANS equations box the first line of boxes represents the turbulence models, while the second line the transition model. The red boxes spotlight the transition models here proposed, as a further development of the $k-\tilde{\omega}$ and Spalart–Allamaras turbulence models. The $k-\tilde{\omega}$ turbulence model are implemented also in the Explicit Algebraic Reynolds Stress Model (EARSM) version. The local and phenomenological $k-k_L-\tilde{\omega}$ and the non-local $\gamma k-\tilde{\omega}$ transition models are yet implemented in the MIGALE solver.

crucial role both in the flow separation and reattachment. Also in the T3C cases, e.g., T3C2, T3C3, and T3C5, the pressure gradient heavily affects the transition.

This testsuite assesses the good prediction capabilities of the proposed transition models, not only with the comparison of the pressure and skin friction coefficient distribution on the wall with experiments and numerical results from literature, but also with the first-order statistics profiles in the domain and the convergence history of the residuals. The high-order accuracy dG solver allows to overcome mesh limits and a strong addiction of the results from the mesh accuracy, but needs corrections of some terms of the formulation of the models to improve the robustness of the convergence.

The main goal of this work is to develop an easy modification of the turbulence models formulation in order to predict transition, i.e., to write transition models without the adding of ad-hoc defined transport equations or the full rewriting of the production and dissipation terms of the working variables. While the secondary goal is, instead, to demonstrate the feasibility of the coupling of transition models with RANS equations in a high-order accuracy dG framework, where already the implementation of a standard turbulence model can prove to be a difficult task for the stiffness associated with the model equations.

Sections 2 and 3 describes the transition model equations, of the SA-BCM and $\gamma k-\tilde{\omega}$ model respectively, while Section 4 the dG spatial discretization of the equations and the pseudo-transient continuation strategy for the steady state solution. Then, Section 5 shows the comparison of the prediction capabilities of the proposed models and other numerical models from literature on the testsuite: Section 5.1 for the ERCOFTAC zero pressure gradient flat plates, Section 5.2 for the ERCOFTAC non-zero pressure gradient flat plates, Section 5.3 for the ERCOFTAC rounded leading-edge flat plates, and Section 5.4 for the Eppler 387 airfoil. Finally, Section 6 summarizes the conclusive remarks of this work.

2. SA-BCM model

The complete set of the incompressible RANS and Spalart–Allmaras BCM transition model [13,14] equations can be written as

$$\frac{\partial u_j}{\partial x_j} = 0, \tag{1}$$

$$\frac{\partial u_i}{\partial t} + \frac{\partial}{\partial x_j}\left(u_j u_i\right) = -\frac{\partial p^*}{\partial x_i} + \frac{\partial \widehat{\tau}^*_{ji}}{\partial x_j}, \tag{2}$$

$$\frac{\partial \tilde{\nu}}{\partial t} + \frac{\partial}{\partial x_j}\left(u_j \tilde{\nu}\right) = \gamma_{BC} c_{b1} \tilde{S} \tilde{\nu} - c_{w1} f_w \left(\frac{\tilde{\nu}}{d}\right)^2 + \frac{1}{\sigma}\left[\frac{\partial}{\partial x_j}\left(\left(\nu + \tilde{\nu}\right)\frac{\partial \tilde{\nu}}{\partial x_j}\right) + c_{b2}\frac{\partial \tilde{\nu}}{\partial x_j}\frac{\partial \tilde{\nu}}{\partial x_j}\right] \tag{3}$$

where the density is a constant and the pressure and the turbulent and total stress tensors are $p^* = p/\rho$, $\widehat{\tau}^*_{ji} = \widehat{\tau}_{ji}/\rho$, and $\tau^*_{ji} = \tau_{ji}/\rho$. The turbulent viscosity and the closure functions are given by

$$\nu_t = \max\left(0, \tilde{\nu}\right) f_{v1}, \qquad f_{v1} = \frac{\chi^3}{\chi^3 + c_{v1}^3}, \qquad \chi = \frac{\tilde{\nu}}{\nu},$$

$$\tilde{S} = \Omega + \frac{\tilde{\nu}}{\kappa^2 d^2} f_{v2}, \qquad f_{v2} = 1 - \frac{\chi}{1 + \chi f_{v1}},$$

$$f_w = g\left[\frac{1 + c_{w3}^6}{g^6 + c_{w3}^6}\right]^{1/6}, \qquad g = r + c_{w2LRe}\left(r^6 - r\right).$$

where $\tilde{\nu}$ is kept non negative in the turbulent viscosity. $\Omega = \sqrt{2\Omega_{ij}\Omega_{ij}}$ is the vorticity magnitude and Ω_{ij} the vorticity tensor. The formulation of r is modified according to Crivellini et al. [4] as

$$r = \begin{cases} \max(r^*, r_{max}) & r^* < 0 \\ \min(r^*, r_{max}) & r^* \geq 0, \end{cases} \qquad r^* = \frac{\tilde{\nu}}{\tilde{S}\kappa^2 d^2}, \tag{4}$$

which avoids the sign inversion of the source terms and greatly improves the robustness of the convergence, especially for high-order solvers.

The intermittency function γ_{BC} is defined as

$$\gamma_{BC} = 1 - \exp\left(-\sqrt{Term_1} - \sqrt{Term_2}\right), \tag{5}$$

with two different functions, e.g., the $Term_1$ and $Term_2$, defined as

$$Term_1 = \frac{\max\left(Re_\theta - Re_{\theta c}, 0\right)}{\chi_1 Re_{\theta c}}, \qquad Term_2 = \max\left(\frac{\nu_t}{\chi_2 \nu}, 0\right), \tag{6}$$

where $Re_\theta = Re_{d^2\Omega}/2.193$ is the momentum thickness Reynolds number and $Re_{d^2\Omega} = d^2\Omega/\nu$ is the vorticity Reynolds number. The threshold value $Re_{\theta c}$ is a critical momentum thickness Reynolds number, which is written with a formulation based on experiments, i.e.,

$$Re_{\theta c} = 803.73\left(Tu_\infty + 0.6067\right)^{-1.027}.$$

Table 1
Constants of the SA-BCM model.

$\chi_1 = 0.002$	$\chi_2 = 50$	$r_{max} = 10^3$
$c_{b1} = 0.1355$	$c_{b2} = 0.622$	$\sigma = 2/3$
$c_{w1} = \frac{c_{b1}}{\kappa^2} + \frac{1+c_{b2}}{\sigma}$	$c_{w3} = 2$	$c_{w4} = 0.21$
$c_{w5} = 1.5$	$c_{v1} = 7.1$	$\kappa = 0.41$

Table 2
Constants of the $\gamma k - \tilde{\omega}$ model, where only the constants of the transitional model are here reported. While α, α^*, β, β^*, σ and σ^* are the constants of the original $k-\tilde{\omega}$ model [7].

$A_0 = 4.04$	$A_S = 2.12$	$A_v = 5.20$
$A_{TH1} = 0.2$	$A_{TH2} = 0.2$	$A_{TH3} = 0.1$
$C_{TH1} = 21$	$C_{TH2} = 1.05$	$C_{TH3} = 0.002$
$C_S = 1.7$	$C_\lambda = 2.495$	$C_{INT} = 0.95$
$C_{\mu,std} = 0.09$	$C_k = 6$	$C_\chi = 10$
$A_{SI} = 1000$	$C_{SI} = 2$	$C_{Kleb} = 1/2$
$c_\omega = 2$	$b_\gamma = 150$	$a_\gamma = 0.95$
$a_\omega = 20$	$b_\omega = 5$	$\chi_1 = 0.002$
$\chi_2 = 50$	Pr = 0.72	$\mathrm{Pr}_t = 0.85$

$Term_1$ is mainly responsible for the production of the intermittency function, in fact starts the production which is supported downstream by the $Term_2$ (see Figs. 25 and 26). Due to the fact that the vorticity Reynolds number is based also on the distance from the wall, the intermittency function takes a very low value inside the boundary layer. As a consequence, $Term_1$ is not able to generate intermittency inside the boundary layer, and $Term_2$ has been added recently [13,14] to overcome this limitation. The transition model constants are tabulated in Table 1.

The model constant c_{w2} is replaced by c_{w2LRe} according to Spalart and Garbaruk [21], defined as

$$c_{w2LRe} = c_{w4} + \frac{c_{w5}}{\left(\frac{\chi}{40}+1\right)^2}, \tag{7}$$

to introduce the dependence from the turbulence model working variable χ. This correction allows to improve the behavior of the model at relatively low Reynolds number, and for this reason, is here implemented. In fact, transitional flows applications take place in low to moderate Reynolds number flows.

In the original model [13,14] the freestream working variable $\tilde{\nu}_\infty$ is set from 0.015ν to 0.025ν. Instead, the influence of the freestream turbulent intensity Tu_∞ is taken into account through the critical momentum thickness Reynolds number $Re_{\theta c}$, and not by the freestream working variable $\tilde{\nu}_\infty/\nu$. The results of all the cases here simulated show how the choice of the freestream working variable can affect the accuracy of the solution. It is quite natural to conjecture that Tu_∞ and $\tilde{\nu}_\infty/\nu$ are somehow related, but, as the Spalart–Allmaras is a one equation model, it is difficult to provide a reliable correlation between these two quantities. From this point of view, the $\gamma k - \tilde{\omega}$ model is completely different, i.e., the freestream turbulent intensity Tu_∞ is imposed through the values of the turbulent variables k_∞ and $\tilde{\omega}_\infty$ at the boundaries of the domain. Finally, the standard $\tilde{\nu}_{wall} = 0$ condition is used at the wall boundaries.

3. $\gamma k - \tilde{\omega}$ Model

The complete set of the compressible RANS and $\gamma k - \tilde{\omega}$ transition model equations can be written as

$$\frac{\partial \rho}{\partial t} + \frac{\partial}{\partial x_j}(\rho u_j) = 0, \tag{8}$$

$$\frac{\partial}{\partial t}(\rho u_i) + \frac{\partial}{\partial x_j}(\rho u_j u_i) = -\frac{\partial p}{\partial x_i} + \frac{\partial \hat{\tau}_{ji}}{\partial x_j}, \tag{9}$$

$$\frac{\partial}{\partial t}(\rho E) + \frac{\partial}{\partial x_j}(\rho u_j H) = \frac{\partial}{\partial x_j}\left[u_i \hat{\tau}_{ij} - \hat{q}_j\right] - \gamma_i f_W f_{SS} f_v C_\mu \tau_{ij} \frac{\partial u_i}{\partial x_j} + \\ - \max\left[\left(1-\gamma_i\right)\max\left(2.8 Tu_\infty \mu - \overline{\mu_T}, 0\right) C_{SI} F_{SI} S^2, C_{Kleb} f_{Kleb} k S\right] \\ + \beta^* \rho \bar{k} e^{\tilde{\omega}_r}, \tag{10}$$

$$\frac{\partial}{\partial t}(\rho k) + \frac{\partial}{\partial x_j}(\rho u_j k) = \frac{\partial}{\partial x_j}\left[(\mu + \sigma^* \overline{\mu_T})\frac{\partial k}{\partial x_j}\right] + \gamma_i f_W f_{SS} f_v C_\mu \tau_{ij} \frac{\partial u_i}{\partial x_j} \\ + \max\left[\left(1-\gamma_i\right)\max\left(2.8 Tu_\infty \mu - \overline{\mu_T}, 0\right) C_{SI} F_{SI} S^2, C_{Kleb} f_{Kleb} k S\right] \\ - \beta^* \rho \bar{k} e^{\tilde{\omega}_r}, \tag{11}$$

$$\frac{\partial}{\partial t}(\rho \tilde{\omega}) + \frac{\partial}{\partial x_j}(\rho u_j \tilde{\omega}) = \frac{\partial}{\partial x_j}\left[(\mu + \sigma \overline{\mu}_T)\frac{\partial \tilde{\omega}}{\partial x_j}\right] + \gamma_i f_W f_{SS} f_v C_\mu \frac{\alpha}{\bar{k}} \tau_{ij} \frac{\partial u_i}{\partial x_j} \\ - \beta \rho e^{\tilde{\omega}_r} + \left(\mu + \sigma \overline{\mu}_T\right)\frac{\partial \tilde{\omega}}{\partial x_k}\frac{\partial \tilde{\omega}}{\partial x_k}, fg \tag{12}$$

where the pressure p, the turbulent and total stress tensors τ_{ij} and $\hat{\tau}_{ij}$, the heat flux vector $\hat{q}_j$, the total specific energy E, and the turbulent viscosity $\overline{\mu}_T$ are given by

$$p = (\gamma_g - 1)\rho\left(E - u_k u_k/2\right), \qquad \hat{q}_j = -\left(\frac{\mu}{\mathrm{Pr}} + \frac{\overline{\mu_T}}{\mathrm{Pr}_t}\right)\frac{\partial h}{\partial x_j},$$

$$E = e + u_k u_k/2,$$

$$\tau_{ij} = 2\overline{\mu_T}\left[S_{ij} - \frac{1}{3}\frac{\partial u_k}{\partial x_k}\delta_{ij}\right] - \frac{2}{3}\rho \bar{k}\delta_{ij}, \qquad \hat{\tau}_{ij} = 2\mu\left[S_{ij} - \frac{1}{3}\frac{\partial u_k}{\partial x_k}\delta_{ij}\right] + \tau_{ij},$$

$$\overline{\mu_T} = \alpha^* \rho \bar{k} e^{-\tilde{\omega}_r},$$

where $\tilde{\omega} = \log(\omega)$, $\bar{k} = \max(0, k)$, γ_g is the ratio of gas specific heats, and Pr and Pr_t are the molecular and turbulent Prandtl numbers. The use of the logarithm of the turbulent variables was introduced by Ilinca and Pelletier [22] for the $k-\epsilon$ model and it is useful to guarantee the positivity of the variables. Moreover, the distribution of the logarithm of the turbulent variables is much smoother than that of the turbulent variables themself. Bassi et al. [7,23–25] proved that, applying the idea of logarithmic variables to the $k-\omega$ model, the logarithm of ω is much more useful than the logarithm of k. Instead, a limit to zero, and not to an arbitrary small value, is used to deal with possible negative values of the turbulent kinetic energy k.

The variable $\tilde{\omega}$ in the source terms and in the turbulent viscosity is replaced by $\tilde{\omega}_r$, to fulfill suitably defined "realizability" conditions [7]. The same turbulent viscosity $\overline{\mu_T}$ is here used in the transition, or turbulence, model equations and Navier–Stokes equations, differently to Kubacki et al. [10–12]. The transition model constants are tabulated in Table 2.

The bypass transition prediction capabilities of this model are represented by different damping functions, e.g., the shear-sheltering f_{SS}, the wall f_W and the viscous f_v function, the turbulent viscosity coefficient C_μ and the intermittency function. In comparison with the original $\gamma k - \omega$ model proposed by Kubacki et al. [10–12] and Holman and Fürst [8,9], where only the shear sheltering function is defined, here several damping functions are added according to the local and phenomenological $k - k_L - \tilde{\omega}$ transition model, proposed by Walters et al. [6,26] and more recently by Lorini et al. [27,28]. This model considers two different contributions to the turbulent kinetic energy: the small-scale energy k_s, and large-scale energy k_l. The former interacts with the mean-flow as a typical turbulence energy, whereas the latter only contributes to the production of the laminar kinetic energy. The production term of the turbulent kinetic energy is defined as $P_k = \tau_{ij,s}\partial u_i/\partial x_j$ with $\tau_{ij,s} \propto \nu_{T,s}$ and

$$\nu_{T,s} = f_v f_{INT} C_\mu \sqrt{k_s}\lambda_{eff}, \qquad k_s = f_{SS} f_W \bar{k}, \tag{13}$$

where $P_k \propto f_{INT} C_\mu f_{SS} f_W k$. In order to compare the production term of the original $\gamma k - \omega$ and the $k - k_L - \tilde{\omega}$ models can be noticed that both terms are proportional to the turbulent kinetic energy and the shear-sheltering damping function. Furthermore, the intermittency damping function f_{INT} of the $k - k_L - \tilde{\omega}$ model, i.e.,

$$f_{INT} = \min\left(\frac{\bar{k}}{C_{INT} k_{TOT}}, 0\right), \qquad k_{TOT} = \bar{k} + \overline{k_L}, \tag{14}$$

is very closed to the definition of the intermittency, i.e., $\overline{k}/k_{TOT}$, modeled in the $\gamma k-\omega$ model. In fact, the intermittency models the transition of the flow, representing the part of the turbulent kinetic energy in the total kinetic energy. In the laminar boundary layer, where the intermittency function γ_i and the intermittency damping function f_{INT} are zero, all the total kinetic energy is given by the laminar kinetic energy k_L, while in the turbulent boundary layer the functions become one and the turbulent kinetic energy correspond to the total kinetic energy of the flow. The similarities between the original $\gamma k-\omega$ model and the $k-k_L-\tilde{\omega}$ model allow to develop an improved version of the $\gamma k-\omega$ model, where also the wall and the viscous damping functions and the turbulent viscosity coefficient are introduced in the production term of the turbulent kinetic energy.

The kinematic wall effect is included through an effective wall-limited turbulent length scale λ_{eff} and the wall damping function f_W, as

$$\lambda_{eff}=\min\left(C_\lambda d,\lambda_T\right),\qquad f_W=\left(\frac{\lambda_{eff}}{\lambda_T}\right)^{\frac{2}{3}}, \tag{15}$$

where $\lambda_T=\sqrt{\overline{k}}/\omega$ is the turbulent length scale, d is the wall distance and C_λ is a model constant. The viscous wall effect is incorporated through a viscous damping function defined as

$$f_v=1-\exp\left(-\frac{\sqrt{Re_T}}{A_v}\right), \tag{16}$$

where $Re_T=f_W^2\overline{k}/\left(\nu e^{\tilde{\omega}}\right)$ is the effective turbulence Reynolds number and A_v a model constant. To satisfy the realizability constraint suggested by Shih et al. [29], the turbulent viscosity coefficient takes the form

$$C_\mu=\frac{1}{A_0+A_S\left(\frac{S}{e^{\tilde{\omega}}}\right)}, \tag{17}$$

where A_0 and A_S are model constants. The shear-sheltering effect is included through the damping function f_{SS} that can be alternatively defined with different characteristic Reynolds number, as

$$Re_{k\Omega}=\frac{\overline{k}}{\nu\Omega},\qquad f_{SS}=\exp\left[-\left(C_{SS}\frac{\nu\Omega}{\overline{k}}\right)^2\right], \tag{18}$$

$$Re_{\sqrt{k}d}=\frac{\sqrt{\overline{k}}d}{\nu},\qquad f_{SS}=\exp\left[-\left(C_{SS}\frac{\nu}{\sqrt{\overline{k}}d}\right)^2\right], \tag{19}$$

according to the improvement proposed by Walters and Cokljat [26–28].

Kubacki et al. in [12] introduced a modification of the model constant C_{SS} to take into account damping or amplification of Klebanoff streaks in accelerating or decelerating flows, for example due to geometry of separation bubbles. In particular

$$C_{SS}=C_S\left(1+f_k\chi\right), \tag{20}$$

$$\chi=tanh\left[\frac{-\Omega\left(S-\Omega\right)}{C_\chi\left(\beta^* e^{\tilde{\omega}}\right)^2}\right],\qquad f_k=1-tanh\left(\frac{\overline{k}}{C_k\nu e^{\tilde{\omega}}}\right), \tag{21}$$

where the C_S, C_χ and C_k are model constants. The effect of acceleration, or deceleration, is taken into account by the χ function, which is positive in accelerating flow due to the curvature, and increases the model constant, thus enlarging the shear sheltering and delaying the transition. The f_k function equals unity near the walls and becomes zero away from walls, and allows to limit the modification of the model constant to the middle part of a pre-transitional boundary layer. C_{SS} is larger in the middle part of a pre-transitional boundary layer in an accelerating flow due to curvature, and the reduction is very small in a decelerating flow. This modification damps or amplifies the Klebanoff streaks, where Zaki et al. [30] showed that Klebanoff streaks are damped in the front part of the suction side of a compressor blade due to strong local flow acceleration, with a delayed transition with respect to the transition on the pressure side of the blade.

3.1. The separation-induced transition production term

The separation-induced production term of the turbulent kinetic energy can be written as

$$P_{SI}=(1-\gamma)\max\left(2.8Tu_\infty\mu-\overline{\mu_T},0\right)C_{SI}F_{SI}S^2, \tag{22}$$

where

$$Re_{d^2S}=\frac{Sd^2}{\nu},\qquad F_{SI}=\exp\left[-\left(\frac{A_{SI}}{Re_{d^2S}}\right)\right]=\exp\left[-\left(A_{SI}\frac{\nu}{Sd^2}\right)\right]. \tag{23}$$

In comparison with Kubacki et al. [12], where $P_{SI}=(1-\gamma)C_{SI}F_{SI}\mu S^2$ and $F_{SI}=\min\left[\max\left(Re_{d^2S}/\left(2.2A_{SI}\right)-1,0\right),1\right]$, the term here proposed adds an exponential function to increase the smoothness, similarly to the intermittency and the shear-sheltering damping functions. $\max\left(2.8Tu_\infty\mu-\overline{\mu_T}\right)$ term is added to limit the production of the turbulent kinetic energy downstream near the reattachment region of the flow, and is similar to the term proposed by Menter et al. [5]. In particular, 3μ is replaced with $2.8Tu_\infty\mu$ to introduce an influence of the freestream turbulent intensity also in the separation-induced transition cases. Furthermore, without this term and in plates with a blunt leading edge, there is an unphysical creation of turbulence due to normal straining, and this is important for low freestream turbulence intensities, where the turbulent intensity in the separation region shows an over-prediction [9].

The function F_{SI} guarantees that the production of the turbulent kinetic energy is only active for sufficiently large values of the Strain-rate Reynolds number Re_{d^2S}. In the formulation of the separation-induced production term an essential role is played by the shear term μS^2, which becomes active in a separated boundary layer at low freestream turbulent intensity levels. This term effectively boosts turbulence production, allowing fast transition and turbulent boundary layer reattachment. Alternatively, μS^2 can be substituted with $\mu S\Omega$, according to Menter et al. [5], or $\overline{k}S$, to emphasize the proportionality between the production term and the turbulent kinetic energy.

Recently, Kubacki et al. in [12] introduced a minimum intensity of the production term of the turbulent kinetic energy due to separation-induced transition, where this term is rewritten as the maximum function between two different contributions to the production of the turbulent kinetic energy, i.e., $P_{SI}=\max\left(P_{SI1},P_{SI2}\right)$, where

$$P_{SI1}=(1-\gamma)\max\left(2.8Tu_\infty\mu-\overline{\mu_T},0\right)C_{SI}F_{SI}\mu S^2, \tag{24}$$

$$P_{SI2}=C_{Kleb}f_{Kleb}\overline{k}S. \tag{25}$$

The first term P_{SI1} correspond to the original P_{SI} term and represents the breakdown of the separated shear layer due to the Kelvin–Helmholtz instabilities under low freestream turbulent intensities, while the second term P_{SI2} adjusts the production for moderate and high intensities. In fact, with an higher level of turbulent intensity the Klebanoff streaks helps the transition mechanism also for the separation-induced transition mode. The f_{Kleb} function, which detects a separated shear layer similarly to F_{SI}, is given by three different functions, i.e., $f_{Kleb}=f_\gamma f_\omega f_w$, defined as

$$f_\gamma=\frac{1}{1+\exp\left[b_\gamma\left(\gamma-a_\gamma\right)\right]}, \tag{26}$$

$$f_\omega=\frac{1}{1+\exp\left[-b_\omega\left(Re_\omega-a_\omega\right)\right]}=\frac{1}{1+\exp\left[-b_\omega\left(\frac{e^{\tilde{\omega}}d^2}{\nu}-a_\omega\right)\right]}, \tag{27}$$

$$f_w=\exp\left[-\left(\frac{Re_T}{c_w}\right)^2\right], \tag{28}$$

where $Re_\omega=e^{\tilde{\omega}}d^2/\nu$ [12]. The F_{SI} is active in a separated boundary layer and contributes to the production of the turbulent kinetic energy when the local turbulence level is very low. While the product of the f_γ and f_ω functions becomes different from zero in the outer zone of a separated laminar boundary layer under moderate or high free-stream turbulent intensity.

3.2. The intermittency function

The activation of the intermittency function represents the excitation of the streaks by the fine turbulence scales in the edge zone of a laminar boundary layer, which leads to the breakdown of the boundary layer and the transition. After transition, the intermittency becomes one in the turbulent part of a turbulent boundary layer. It stays zero at the wall and evolves towards unity inside the viscous sublayer, where the formulation influences the growth inside the boundary layer. The intermittency function is traditionally defined according to the definition of the shear-sheltering function [9–12], i.e., to the characteristic Reynolds number used in the shear-sheltering function, as

$$Re_{\sqrt{k}\,d} = \frac{\sqrt{\overline{k}}d}{\nu}, \qquad \gamma_1^* = \min\left(\max\left(\frac{\sqrt{\overline{k}}d}{\nu} - C_{TH\,1}, 0\right), 1\right), \tag{29}$$

$$Re_{k\,\Omega} = \frac{\overline{k}}{\nu\Omega}, \qquad \gamma_2^* = \min\left(\max\left(\frac{\overline{k}}{\nu\Omega} - C_{TH\,2}, 0\right), 1\right), \tag{30}$$

where C_{TH} is the threshold value of transition and the wall-distance and turbulent kinetic energy Reynolds numbers, $Re_{\sqrt{k}\,d}$ and $Re_{k\Omega}$, work here as threshold parameter. According to Kubacki et al. [31], the intermittency formulation can be also based on the dissipation rate of the turbulent kinetic energy, as

$$Re_{k\omega} = \frac{\overline{k}e^{\tilde{\omega}_r}}{\nu\Omega^2}, \qquad \gamma_3^* = \min\left(\max\left(\frac{\overline{k}e^{\tilde{\omega}_r}}{\nu\Omega^2} - C_{TH\,3}, 0\right), 1\right). \tag{31}$$

An exponential law is here used to improve the smoothness of the intermittency function and the transition, i.e., $\gamma_i = 1 - \exp\left(\gamma_i^*/A_{TH\,i}\right)$.

Furthermore, the performance of these formulations is compared with an alternative formulation from the Spalart–Allmaras BCM transition model [13,14], here called γ_4. In particular the γ_{BC} intermittency function is rewritten for the $\gamma k - \tilde{\omega}$ model as

$$\gamma_4 = 1 - \exp\left(-\sqrt{Term_1} - \sqrt{Term_2}\right), \tag{32}$$

$$Term_1 = \frac{\max\left(Re_\theta - Re_{\theta c}, 0\right)}{\chi_1 Re_{\theta c}}, \qquad Term_2 = \max\left(\frac{\overline{\nu}_T}{\chi_2\nu}, 0\right),$$

$$Re_\theta = \frac{Re_{d^2\Omega}}{0.25}, \qquad \overline{\nu}_T = \frac{\overline{\mu}_T}{\rho} = \alpha^*\overline{k}e^{-\tilde{\omega}_r},$$

$$Re_{\theta c} = 803.73\left(Tu_\infty + 0.6067\right)^{-1.027}.$$

Both the production terms of the turbulent kinetic energy and the specific dissipation rate are damped by the intermittency function, differently from the models proposed by Holman and Fürst [9] and Kubacki et al. [10,11]. In fact, as spotlighted by Lorini et al. [27,28], the intermittency function in the production term of the specific dissipation rate avoids shorter transition flow regions. The same intermittency function is used for both production terms without any range constraint, differently to [27,28]. The intermittency function is also activated when a large value of the turbulent kinetic energy appears together with a relatively large value of the distance to the wall, which occurs with a large separation zone caused by a very strong adverse pressure gradient combined with a high freestream turbulence level.

3.3. Boundary conditions

At solid walls the homogeneous Neumann condition for the specific dissipation rate $\partial\omega/\partial n = 0$ is prescribed, as suggested in [26]. Furthermore, since the velocity is equal to zero due to the no-slip condition, the turbulent kinetic energy at the wall is also zero. At freestream the specific dissipation rate and turbulent kinetic energy values are computed according to the definition of freestream turbulent intensity and turbulent viscosity ratio as

$$Tu_\infty = \sqrt{\frac{2}{3}\frac{k_\infty}{u_{ref}^2}}, \qquad \left(\frac{\overline{\mu_T}}{\mu}\right)_\infty = \frac{C_\mu k_\infty}{e^{\tilde{\omega}_\infty} u_{ref} L_{ref}} Re$$

where u_{ref} and L_{ref} are the reference velocity and length of the case.

4. Numerical framework

The system of governing equations can be written in compact form as

$$\mathbf{P}(\mathbf{w})\frac{\partial \mathbf{w}}{\partial t} + \nabla\cdot\mathbf{F}^{\mathrm{c}}(\mathbf{w}) + \nabla\cdot\mathbf{F}^{\mathrm{v}}(\mathbf{w},\nabla\mathbf{w}) + \mathbf{s}(\mathbf{w},\nabla\mathbf{w}) = \mathbf{0}. \tag{33}$$

where $\mathbf{w} \in \mathbb{R}^m$ is the vector of the m variables, $\mathbf{F}^{\mathrm{c}} \in \mathbb{R}^m \otimes \mathbb{R}^{1,2,3}$ and $\mathbf{F}^{\mathrm{v}} \in \mathbb{R}^m \otimes \mathbb{R}^{1,2,3}$ are the inviscid and viscous flux functions, $\mathbf{s} \in \mathbb{R}^m$ the sum of the transition model source terms and the volume forces terms, and $\mathbf{P}(\mathbf{w}) \in \mathbb{R}^m \otimes \mathbb{R}^m$ a transformation matrix.

Usually, the compressible solver employs the conservative variables $\mathbf{w}_c = [\rho, \rho u_i, \rho E, \rho k, \rho\widetilde{\omega}]^T$, while the incompressible solver the primitive variables $\mathbf{w}_p = [p, u_i, \tilde{\nu}]^T$. The matrix $\mathbf{P}$ reduces to the identity matrix ($\mathbf{P} = \mathbf{I}$) in the former case and to the difference between the identity and a single-entry matrix ($\mathbf{P} = \mathbf{I} - \mathbf{J}^{11}$) in the latter case. Here, the primitive variables $(p, u_i, T, k, \widetilde{\omega})$ and $(p, u_i, \tilde{\nu})$ are used for the compressible and incompressible equations, respectively, to improve the robustness of the convergence.

4.1. Discontinuous Galerkin space discretization

An arbitrary smooth test function $\mathbf{v} = \{v_1, \ldots, v_m\}$ multiplies the Eq. (33), which is integrating by parts an written as

$$\int_\Omega \mathbf{v}\cdot\left(\mathbf{P}(\mathbf{w})\frac{\partial\mathbf{w}}{\partial t}\right)\,\mathrm{d}\Omega - \int_\Omega \nabla\mathbf{v} : \left(\mathbf{F}^{\mathrm{c}}(\mathbf{w}) + \mathbf{F}^{\mathrm{v}}(\mathbf{w},\nabla\mathbf{w})\right)\,\mathrm{d}\Omega$$
$$+ \int_{\partial\Omega} \mathbf{v}\otimes\boldsymbol{n} : \left(\mathbf{F}^{\mathrm{c}}(\mathbf{w}) + \mathbf{F}^{\mathrm{v}}(\mathbf{w},\nabla\mathbf{w})\right)\,\mathrm{d}\sigma + \int_\Omega \mathbf{v}\cdot\mathbf{s}(\mathbf{w},\nabla\mathbf{w})\,\mathrm{d}\Omega = \mathbf{0}, \tag{34}$$

to obtain the weak formulation of the dG discretization, where the domain is approximated with a computational mesh $\mathcal{T}_h = \{K\}$ consisting of a set of non-overlapping and arbitrary shaped elements. $\boldsymbol{n}$ is the unit normal vector to the boundary. A discontinuous finite element space with polynomial functions of degree l continuous only inside each element K is defined on the mesh as

$$\mathbf{V}_h^l \overset{\mathrm{def}}{=} [\mathbb{P}_d^l(\mathcal{T}_h)]^m,$$

$$\mathbb{P}_d^l(\mathcal{T}_h) \overset{\mathrm{def}}{=} \left\{v_h \in L^2(\Omega_h) \,:\, v_h|_K \in \mathbb{P}_d^l(K),\ \forall K \in \mathcal{T}_h\right\}.$$

In the weak form of Eqs. (33), the solution $\mathbf{w}$ and the test function $\mathbf{v}$ are replaced with a finite element approximation $\mathbf{w}_h$ and $\mathbf{v}_h$ respectively, of the space $\mathbf{V}_h^l$. Orthogonal and hierarchical basis functions are defined in the physical reference frame, as a satisfactory basis for the space $\mathbf{V}_h^l$ [7,32]. Any function v_h can be considered as a combination of the elements and of the basis. ϕ_i is the element basis, where $i \in \{1, \ldots, N_{\mathrm{DoF}}^K\}$ and N_{DoF}^K is the number of degrees of freedom of the polynomial space local to an element K, the dG discretization of the compressible RANS consists in seeking the elements $w_{h,1}, \ldots, w_{h,m}$ of $\mathbf{w}_h \in \mathbf{V}_h^k$ such that

$$\sum_{K\in\mathcal{T}_h}\int_K \phi_i P_{j,k}(\mathbf{w}_h)\,\phi_l\frac{\mathrm{d}W_{k,l}}{\mathrm{d}t}\,\mathrm{d}\Omega$$
$$- \sum_{K\in\mathcal{T}_h}\int_K \frac{\partial\phi_i}{\partial x_k}\left(F_{j,k}^{\mathrm{c}}(\mathbf{w}_h) + F_{j,k}^{\mathrm{v}}\left(\mathbf{w}_h, \nabla_h\mathbf{w}_h + \mathbf{r}^g\left(\left[\!\left[\mathbf{w}_h\right]\!\right]\right)\right)\right)\,\mathrm{d}\Omega$$
$$+ \sum_{f\in\mathcal{F}}\int_f \left[\!\left[\phi_i\right]\!\right]_k\left(\widehat{F}_{j,k}^{\mathrm{c}}\left(\mathbf{w}_h^{\pm}\right) + \widehat{F}_{j,k}^{\mathrm{v}}\left(\mathbf{w}_h^{\pm}, \left(\nabla_h\mathbf{w}_h + \eta_f\mathbf{r}^f\left(\left[\!\left[\mathbf{w}_h\right]\!\right]\right)\right)^{\pm}\right)\right)\,\mathrm{d}\sigma$$
$$+ \sum_{K\in\mathcal{T}_h}\int_K \phi_i s_j\left(\mathbf{w}_h, \nabla_h\mathbf{w}_h + \mathbf{r}^g\left(\left[\!\left[\mathbf{w}_h\right]\!\right]\right)\right)\,\mathrm{d}\Omega = 0,$$
$$\forall i \in \{1, \ldots, N_{\mathrm{DoF}}^K\}, \tag{35}$$

where $j = 1, \ldots, m$,

$$w_{h,j} = \phi_l W_{j,l},$$

and $\mathbf{W}$ is the global vector of unknown degrees of freedom. Furthermore, $\mathbf{r}^g$ and $\mathbf{r}^f : [L^1(f)]^{m\times d} \to [\mathbb{P}_d^l(\mathcal{T}_h)]^{m\times d}$ are the global

and local lifting operators used to guarantee a consistent, stable and accurate discretization of the viscous part of the equations [7,32]. As the functional approximation is discontinuous, the flux is not uniquely defined over the elements boundary, and thus a numerical flux vector is suitably defined both for the inviscid and viscous part of the equations.

The inviscid numerical flux is computed from the solution of local Riemann problems in the normal direction at each integration point on elements faces. For the compressible solver, the exact Riemann solver of Gottlieb and Groth [33] is used, while for the incompressible solver, the main idea is to solve, at the interfaces, an exact Riemann problem associated with a local compressibility perturbation of the Euler equations [1,32]. As the perturbation is only included at the level of the flux evaluation, no time derivative for the pressure variable is added to the discrete continuity equation, resulting in a time-consistent algorithm. The viscous part is given by

$$\widehat{\mathbf{F}^{\mathrm{v}}}\left(\mathbf{w}_h^{\pm}, \left(\nabla_h \mathbf{w}_h + \eta_f \mathbf{r}^f\left(\left[\!\left[\mathbf{w}_h\right]\!\right]\right)\right)^{\pm}\right) \stackrel{\mathrm{def}}{=} \left\{\mathbf{F}^{\mathrm{v}}\left(\mathbf{w}_h, \nabla_h \mathbf{w}_h + \eta_f \mathbf{r}^f\left(\left[\!\left[\mathbf{w}_h\right]\!\right]\right)\right)\right\},$$

where η_f is the stability parameter [7,32].

4.2. Implicit solver for the time integration

The discrete problem corresponding to Eq. (35) can be written as

$$\mathbf{M_P}\frac{\mathrm{d}\mathbf{W}}{\mathrm{d}t} + \mathbf{R}(\mathbf{W}) = \mathbf{0}, \tag{36}$$

where $\mathbf{R}$ is the residuals vector and $\mathbf{M_P}$ is the global block diagonal matrix. $\mathbf{M_P}$ is due to the discretization of the first integral of Eq. (35) and couples the degrees of freedom of the different variables within the element of the mesh through the variable transformation matrix $\mathbf{P}$. In particular, Eq. (36) defines a Differential–Algebraic system of Equations (DAEs) for the incompressible solver, and an Ordinary Differential system of Equations (ODEs) for the compressible solver. For steady simulations, these systems of equations are solved by means of a Linearized Backward Euler (LBE) scheme, i.e,

$$\left[\frac{\mathbf{M_P^n}}{\Delta t} + \frac{\partial \mathbf{R}(\mathbf{W}^n)}{\partial \mathbf{W}}\right]\Delta \mathbf{W} = -\mathbf{R}(\mathbf{W}^n). \tag{37}$$

The linear system arising at each time-step is solved with the matrix-based Generalized Minimal RESidual (GMRES) algorithm, where the block Jacobi preconditioner with one block per process ILU(0) is used to make the convergence of the GMRES solver acceptable in problems of practical interest. The linear algebra and parallelization are handled through the PETSc [34] library (Portable Extensible Toolkit for Scientific Computations) and MPI, the standard for message-passing communication.

In order to advance the solution to the steady state, a pseudo-transient continuation strategy is used, with the local time step given by

$$\Delta t_K = \mathrm{CFL}\frac{h_K}{u_c + u_d},$$

$$u_c = |\mathbf{u}| + a, \qquad u_d = 2\frac{\mu_e + \lambda_e}{h_K}, \qquad h_K = d\frac{V_K}{S_K},$$

where u_c and u_d convective and diffusive velocities and h_K, V_K and S_K are the reference dimension of the element K. The coefficients μ_e and λ_e are the effective dynamic viscosity and conductivity, while a is the speed of sound in the compressible solver and the artificial compressibility coefficient in the incompressible solver [4]. All the quantities depending on $\mathbf{w}_h$ are computed from its mean value. Devising an effective and robust strategy to increase the CFL number as the residual decreases is far from trivial, especially for transitional or turbulent simulations, and an empirically determined "CFL law" is here used to speed-up the convergence. It is based on the L^∞ and L^2 norms of the residual and depends on three user-defined parameters. The first and second parameters are $\mathrm{CFL_{min}}$ and $\mathrm{CFL_{max}}$ to set the minimum and maximum limit of the CFL number during the simulation. The third parameter is an exponent α governing the growth rate of the CFL number, where typically $\alpha \leq 1$.

For the compressible solver the "CFL law" is

$$\mathrm{CFL} = \begin{cases} \mathrm{CFL_{min}}/\xi^{\alpha} & \text{if} \quad \xi \leq 1 \\ \min\left(\mathrm{CFL_{exp}} + \beta e^{\alpha \frac{\mathrm{CFL_{min}}}{\beta}(1-\xi)}, \mathrm{CFL_{max}}\right) & \text{if} \quad \xi > 1 \end{cases} \tag{38}$$

where $\mathrm{CFL_{exp}} = \min(1/(2l+1), \mathrm{CFL_{min}})$ is the minimum value between the maximum CFL number proper of an explicit scheme and the user-defined minimum value, $\beta = \mathrm{CFL_{min}} - \mathrm{CFL_{exp}}$, and

$$\xi = \begin{cases} \min(1, \xi_2) & \text{if} \quad \xi_\infty \leq 1, \qquad \xi_2 \stackrel{\mathrm{def}}{=} \max\limits_{i=1,\dots,m}\left(\|R_i\|_2/\|R_{i0}\|_2\right), \\ \xi_\infty & \text{if} \quad \xi_\infty > 1, \qquad \xi_\infty \stackrel{\mathrm{def}}{=} \max\limits_{i=1,\dots,m}\left(\|R_i\|_\infty/\|R_{i0}\|_\infty\right), \end{cases}$$

where $\|\cdot\|_2$ and $\|\cdot\|_\infty$ are the L_2 and L_∞ norms, respectively, R_i is the residual vector of the ith equation of the system, R_{i0} is the corresponding residual at the first iteration. While for the incompressible solver the SA-BCM model allows a simpler formulation, which is

$$\mathrm{CFL} = \max\left(\frac{\mathrm{CFL_{min}}}{\max\left(\xi_2, \xi_\infty\right)^{\alpha}}, \mathrm{CFL_{max}}\right). \tag{39}$$

In fact, the turbulent variables of the $\gamma k - \tilde{\omega}$ model, as well as in the original turbulence model [1,7,32], introduce a lack of robustness and a more sophisticated law is mandatory.

5. Numerical results

The proposed transition models, i.e., the $\gamma k - \tilde{\omega}$ model and the SA-BCM model, are assessed and validated by computing the flow over the flat plates of the ERCOFTAC T3 series with zero and non-zero pressure gradients, investigated experimentally by Coupland [18] and Coupland and Brierley [19]. These test cases are mainly characterized by bypass and separation-induced transition, with different freestream Reynolds number Re_∞ and turbulent intensity at the leading edge of the plate Tu_{LE}. Furthermore the transitional flow around an Eppler 387 airfoil with freestream turbulent intensity $Tu_\infty = 0.1\%$ and Reynolds number $Re_\infty = 200\,000$, based on the chord of the airfoil and the freestream flow quantities, and different angles of attack is considered in comparison with the experiments by McGhee et al. [20] at Langley Low-Turbulence Pressure Tunnel (LTPT). In particular, in the ERCOFTAC zero and non-zero pressure gradient flat plats, e.g., T3A, T3B and T3A- cases with zero pressure gradient and T3C2, T3C3, and T3C5 with non-zero pressure gradient, the transition is in the bypass mode, while in the ERCOFTAC rounded leading edge flat plates, e.g., T3L cases, and in the Eppler 387 airfoil cases the transition is in the separation-induced mode. In the former cases the separation is due to the geometry and only the reattachment has to be triggered by the model, while in the latter case the separation is due to the pressure gradient and the model play a crucial role both in the flow separation and reattachment.

All the simulations are carried out in parallel by initializing the piecewise constant $\mathbb{P}^0$ solution, for the $\gamma k - \tilde{\omega}$ model, and the $\mathbb{P}^1$ solution, for the SA-BCM model, from the uniform flow at the freestream conditions and the higher-order solutions from the lower-order ones. The lower solution approximation of the SA-BCM model is $\mathbb{P}^1$, instead $\mathbb{P}^0$, due to the fact that the solver is incompressible and pressure has a lower by one order of accuracy of the solution.

5.1. Zero pressure gradient flat plates

The T3A, T3B and T3A- flat plates of the ERCOFTAC T3 series with zero pressure gradient are here used to validate and calibrate the transition models with bypass transition. They are characterized by different values of the freestream velocity u_∞ and turbulence intensity at the leading edge of the plate Tu_{LE}, ranging from 0.9% to 6% (see Table 3). The freestream turbulent quantities of the $\gamma k - \tilde{\omega}$ model,

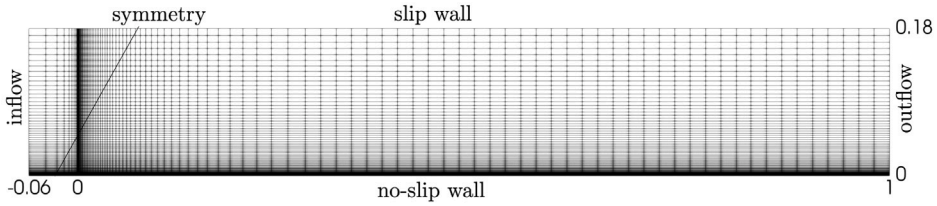

Fig. 2. Zero pressure gradient flat plates. Computational mesh of the T3A, T3B and T3A- cases. The boundary conditions in clockwise direction from the leading edge of the plate $(x, y) = (0, 0)$ are: symmetry, inflow, slip wall (or freestream), outflow, and no-slip wall.

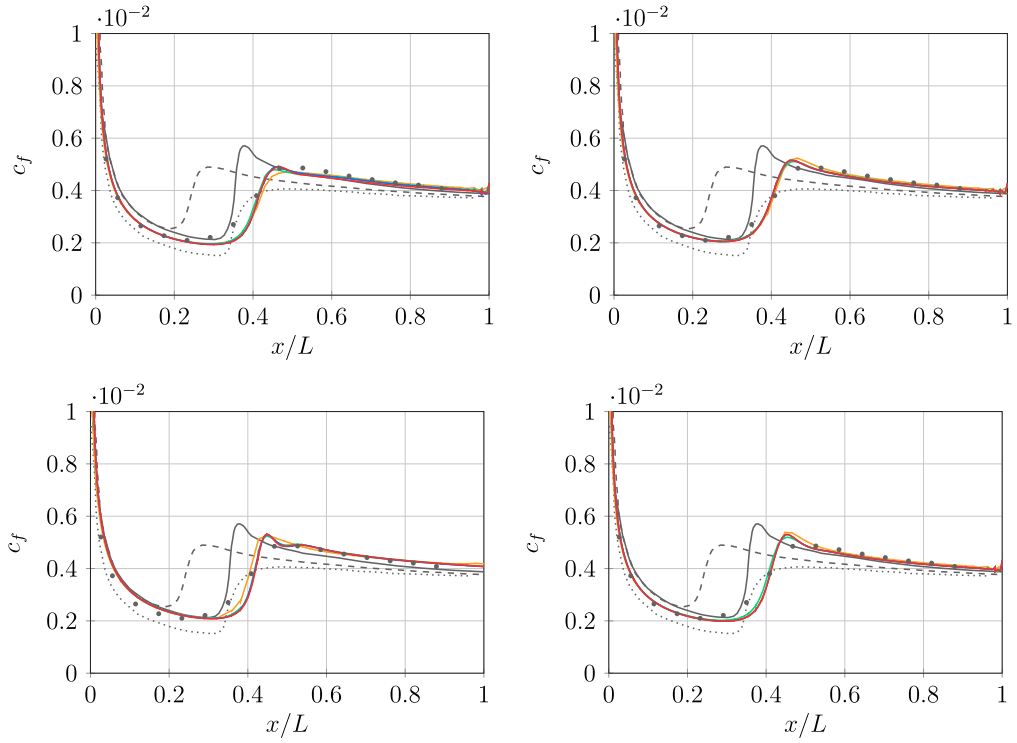

Fig. 3. Zero pressure gradient flat plates. Skin friction coefficient c_f along the plate for the zero pressure gradient T3A flat plate with the $\gamma k - \tilde{\omega}$ model and different intermittency functions: γ_1 (top, left), γ_2 (top, right), γ_3 (bottom, left) and γ_4 (bottom, right), from $\mathbb{P}^1$ to $\mathbb{P}^4$ solution approximation. $DG-\mathbb{P}^1$, $DG-\mathbb{P}^2$, $DG-\mathbb{P}^3$, $DG-\mathbb{P}^4$, Holman and Fürst $\gamma k-\omega$ model, Cakmakcioglu et al. SA-BCM model, Kubacki et al. $\gamma k-\omega$ model, • Coupland exp.

Table 3
Zero pressure gradient flat plates. Flow conditions for the T3A, T3B and T3A- flat plates [18].

	T3A	T3B	T3A-
u_∞ [m/s]	5.4	9.4	19.8
Tu_{LE} [%]	3.0	6.0	0.9

e.g., Tu_∞ and $(\mu_T/\mu)_\infty$, are chosen in order to match the experimental turbulent intensity at the leading edge of the plate and the decay of the turbulent intensity along the domain. The same mesh, made of $n_e = 8800$ quadrilateral elements, is used for all the testcases, where the inflow boundary is set at $x/L = -0.06$ from the leading edge of the plate and adiabatic no-slip wall boundary condition is set on the plate (see Fig. 2). The mesh has $n_x = 100$ number of element in x-direction on the wall, i.e., $x/L > 0$, $n_y = 80$ number of element in y-direction, and $\Delta y_1/L = \Delta x_1/L = 0.0002$ as height and length of the first element from the wall and from the leading edge of the plate in x-direction, respectively. The results of the proposed models are compared with the available experimental data of Coupland [18] and the numerical solution of the $\gamma k-\omega$ model of Holman et al. [8,9], Kubacki et al. [10–12], and the SA-BCM model of Cakmakcioglu et al. [13,14].

With the $\gamma k - \tilde{\omega}$ model all the intermittency functions, e.g. γ_1, γ_2, γ_3, and γ_4 are similar on all the cases, and can be used without significant difference in the solutions. For example, Fig. 3 shows the skin friction coefficient distributions on the T3A plate with different solution approximations and intermittency function formulations. The comparison of an average error respect to the experimental distribution of the skin friction coefficient is out of the goals of this work, and for this reason the accuracy of the different intermittency functions should be considered similar. Instead, the choice of the intermittency function can be based on the convergence speed-up and the robustness of the solver. The γ_2 formulation guarantees more robustness during the convergence and for this reason is used in all the cases. In fact, Fig. 4 shows the convergence history of the $\gamma k-\tilde{\omega}$ model with the same "CFL law", e.g., $\mathrm{CFL}_{\min} = 1$, $\mathrm{CFL}_{\max} = 10^{20}$ and $\alpha = 1$, and the different intermittency functions. Furthermore, γ_2 allows to increase the $\mathrm{CFL}_{\min}$ parameter more than the other formulations and, thus, to reduce the computational cost of the simulation.

Fig. 5 shows the skin friction coefficient distributions on the plate with the $\gamma k - \tilde{\omega}$ model and different solution approximations. Furthermore, Fig. 5 shows also the decay of the turbulent intensity and the x-component velocity along the domain outside of the boundary layer in order to prove the correctness of the boundary conditions of

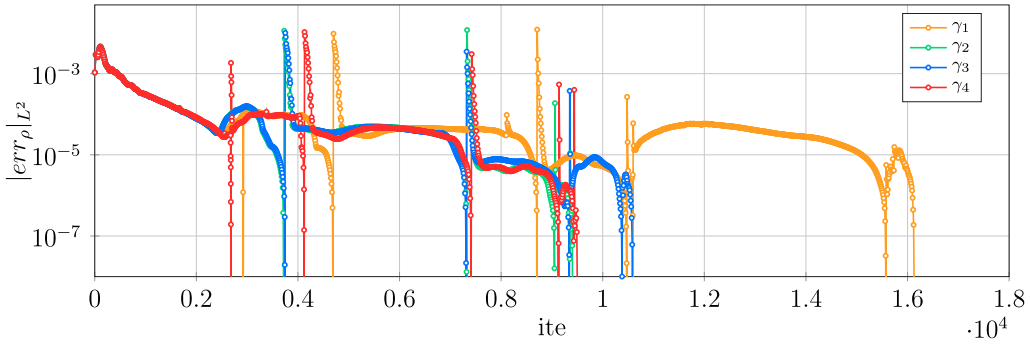

Fig. 4. Zero pressure gradient flat plates. The convergence history, in terms of the L^2 norm of the density residuals, of the $\gamma k - \tilde{\omega}$ transition model, with the different intermittency functions in the T3A case, from $\mathbb{P}^0$ to $\mathbb{P}^4$ solution approximation. In order to have a easy comparison symbols represent 1 iteration of 10.

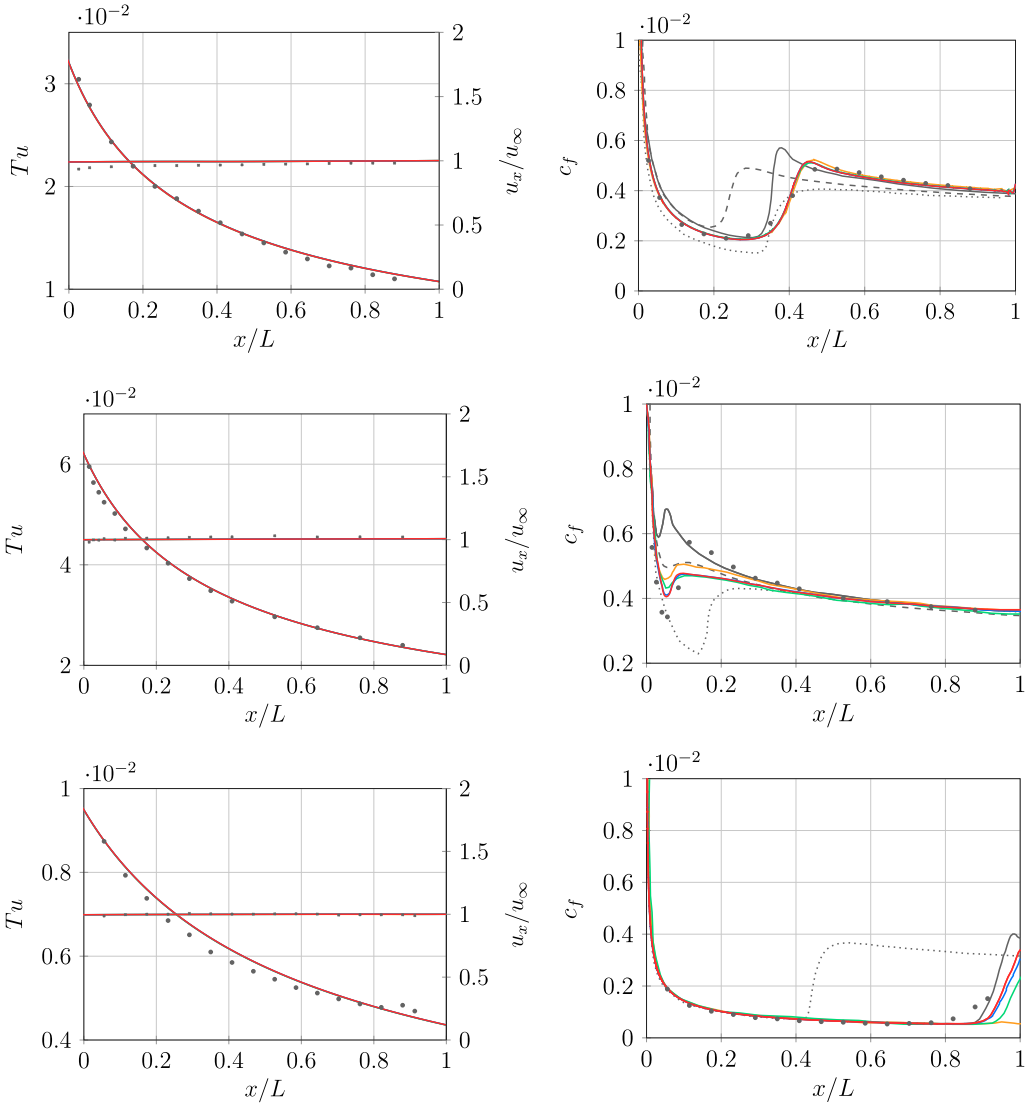

Fig. 5. Zero pressure gradient flat plates. Turbulent intensity Tu and x-component velocity u_x along the domain and skin friction coefficient c_f along the plate for the zero pressure gradient flat plates with the $\gamma k - \tilde{\omega}$ model, T3A (top), T3B and T3A- (bottom), from $\mathbb{P}^1$ to $\mathbb{P}^4$ solution approximation. — $DG - \mathbb{P}^1$, — $DG - \mathbb{P}^2$, — $DG - \mathbb{P}^3$, — $DG - \mathbb{P}^4$, —— Holman and Fürst $\gamma k - \omega$ model, ····· Cakmakcioglu et al. SA-BCM model, – – – Kubacki et al. $\gamma k - \omega$ model, • Coupland exp.

the turbulent quantities. While Figs. 6 and 7 show the skin friction coefficient distributions on the plate with the SA-BCM model and different solution approximations and values of the freestream working variable $\tilde{\nu}_\infty/\nu = 1.5 \times 10^i$ with $i = \{0, \dots, -15\}$, respectively.

Regarding the $\gamma k - \tilde{\omega}$ model the solutions of the skin friction coefficient are almost overlapped with experiments in the T3A and T3A- case, where starting from $\mathbb{P}^2$ approximation the solution has no significant difference increasing the accuracy. In the T3B case the skin friction

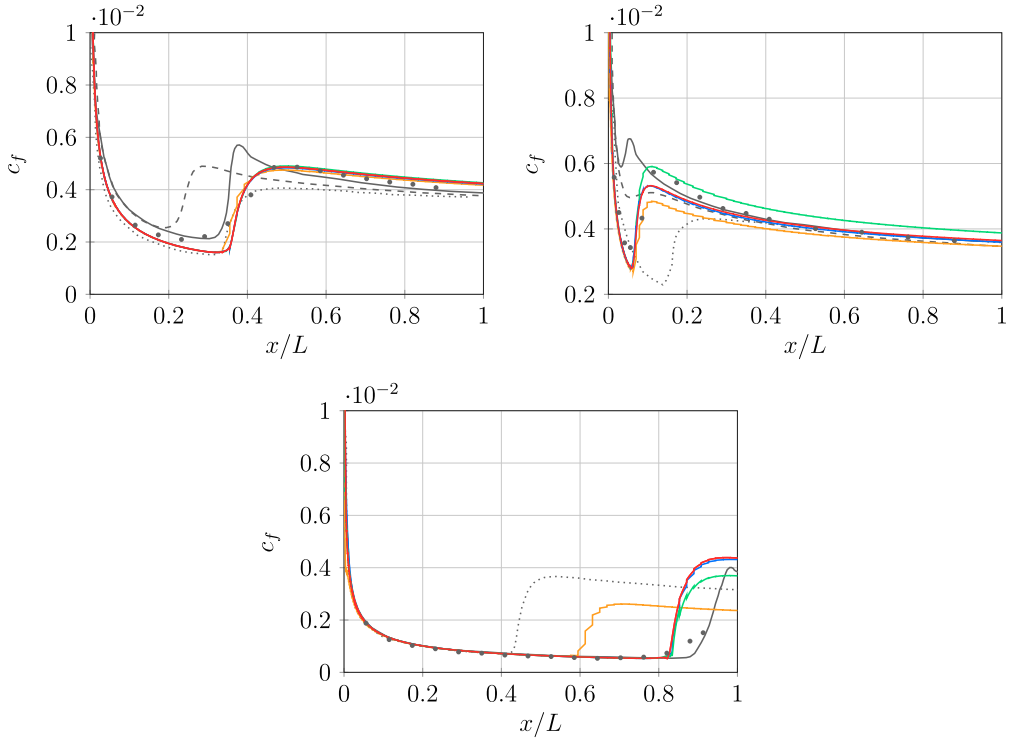

Fig. 6. Zero pressure gradient flat plates. Skin friction coefficient c_f along the plate for the zero pressure gradient flat plates with the SA-BCM model, T3A (top, left), T3B (top, right) and T3A- (bottom), from $\mathbb{P}^1$ to $\mathbb{P}^4$ solution approximation. The solutions are here reported with the best values of the freestream working variables, e.g., $\tilde{\nu}_\infty/\nu = 1.5 \times 10^{-2}$, 1.5×10^{-1} and 1.5×10^{-14} for T3A, T3B and T3A-, respectively. — $DG-\mathbb{P}^1$, — $DG-\mathbb{P}^2$, — $DG-\mathbb{P}^3$, — $DG-\mathbb{P}^4$, — Holman and Fürst $\gamma k-\omega$ model, ····· Cakmakcioglu et al. SA-BCM model, – – – Kubacki et al. $\gamma k-\omega$ model, • Coupland exp.

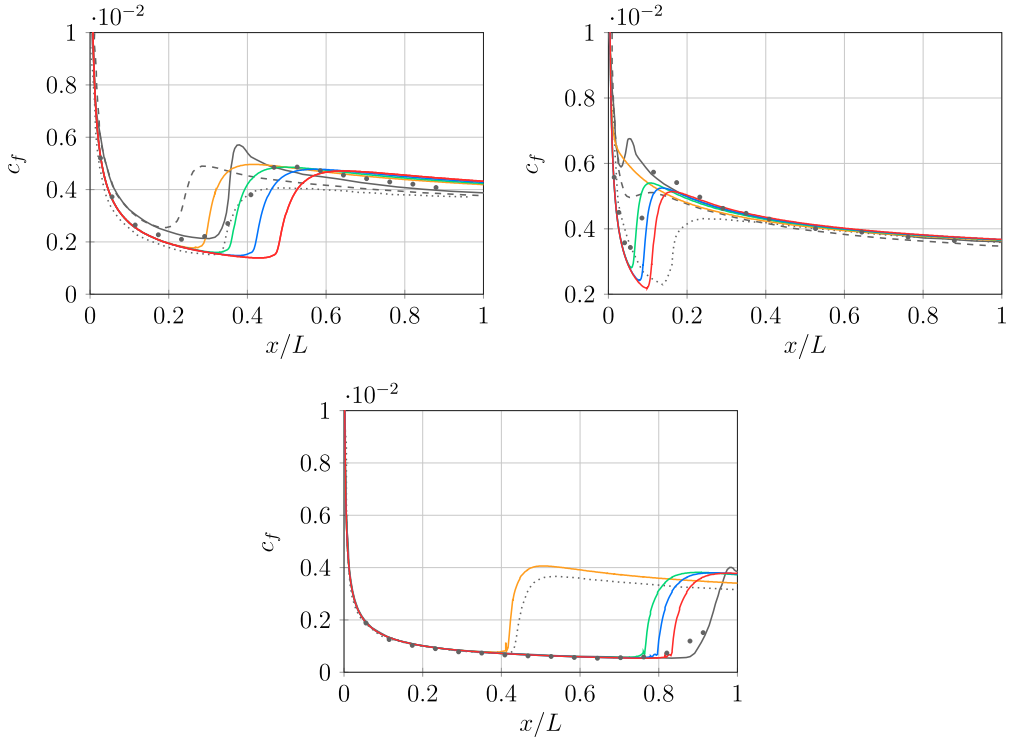

Fig. 7. Zero pressure gradient flat plates. Skin friction coefficient c_f along the plate for the zero pressure gradient flat plates with the SA-BCM model and different freestream working variables $\tilde{\nu}_\infty$, T3A (top, left), T3B (top, right) and T3A- (bottom), $\mathbb{P}^4$ solution approximation. T3A: — $\tilde{\nu}_\infty/\nu = 1.5\times10^{-1}$, — $\tilde{\nu}_\infty/\nu = 1.5\times10^{-2}$, — $\tilde{\nu}_\infty/\nu = 1.5\times10^{-3}$, — $\tilde{\nu}_\infty/\nu = 1.5\times10^{-4}$, — Holman and Fürst $\gamma k-\omega$ model, ····· Cakmakcioglu et al. SA-BCM model, – – – Kubacki et al. $\gamma k-\omega$ model, • Coupland exp. T3B: — $\tilde{\nu}_\infty/\nu = 1.5\times10^{0}$, — $\tilde{\nu}_\infty/\nu = 1.5\times10^{-1}$, — $\tilde{\nu}_\infty/\nu = 1.5\times10^{-2}$, — $\tilde{\nu}_\infty/\nu = 1.5\times10^{-3}$, — Holman and Fürst $\gamma k-\omega$ model, ····· Cakmakcioglu et al. SA-BCM model, – – – Kubacki et al. $\gamma k-\omega$ model, • Coupland exp. and T3A-: — $\tilde{\nu}_\infty/\nu = 1.5\times10^{-2}$, — $\tilde{\nu}_\infty/\nu = 1.5\times10^{-12}$, — $\tilde{\nu}_\infty/\nu = 1.5\times10^{-13}$, — $\tilde{\nu}_\infty/\nu = 1.5\times10^{-14}$, — Holman and Fürst $\gamma k-\omega$ model, ····· Cakmakcioglu et al. SA-BCM model, – – – Kubacki et al. $\gamma k-\omega$ model, • Coupland exp.

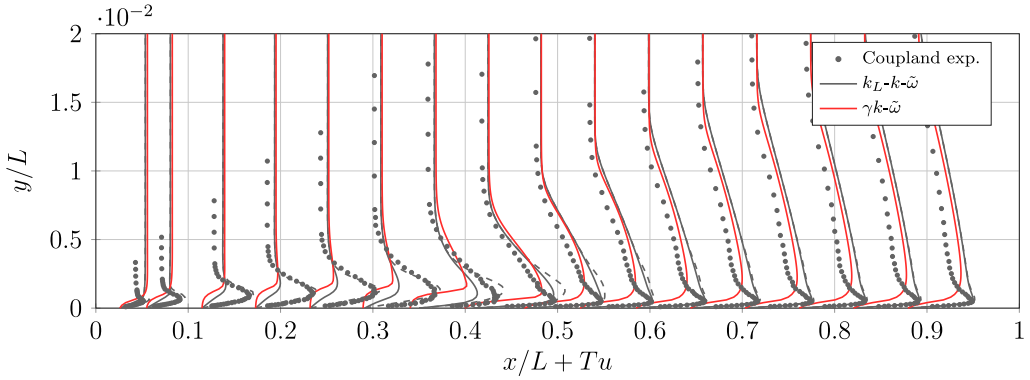

Fig. 8. Zero pressure gradient flat plates. Turbulent intensity $Tu = \sqrt{2/3k}/u_\infty$ at different locations x/L along the domain with the $\gamma k - \tilde{\omega}$ model and the $k_L - k - \tilde{\omega}$ model [27,28] in the T3A case, $\mathbb{P}^4$ solution approximation. For the Coupland experiments [18] only the x-component velocity fluctuations are here considered, i.e., $Tu = \sqrt{\overline{u_x'^2}/3}/u_\infty$, in fact the y- and z-component are negligible. For the $k_L - k - \tilde{\omega}$ [27,28] transition model the dashed lines represent the turbulent intensity based on the total kinetic energy $Tu = \sqrt{2/3k_{TOT}}/u_\infty$ and $k_{TOT} = k + k_L$, while the solid lines the turbulent intensity based on the turbulent kinetic energy $Tu = \sqrt{2/3k}/u_\infty$.

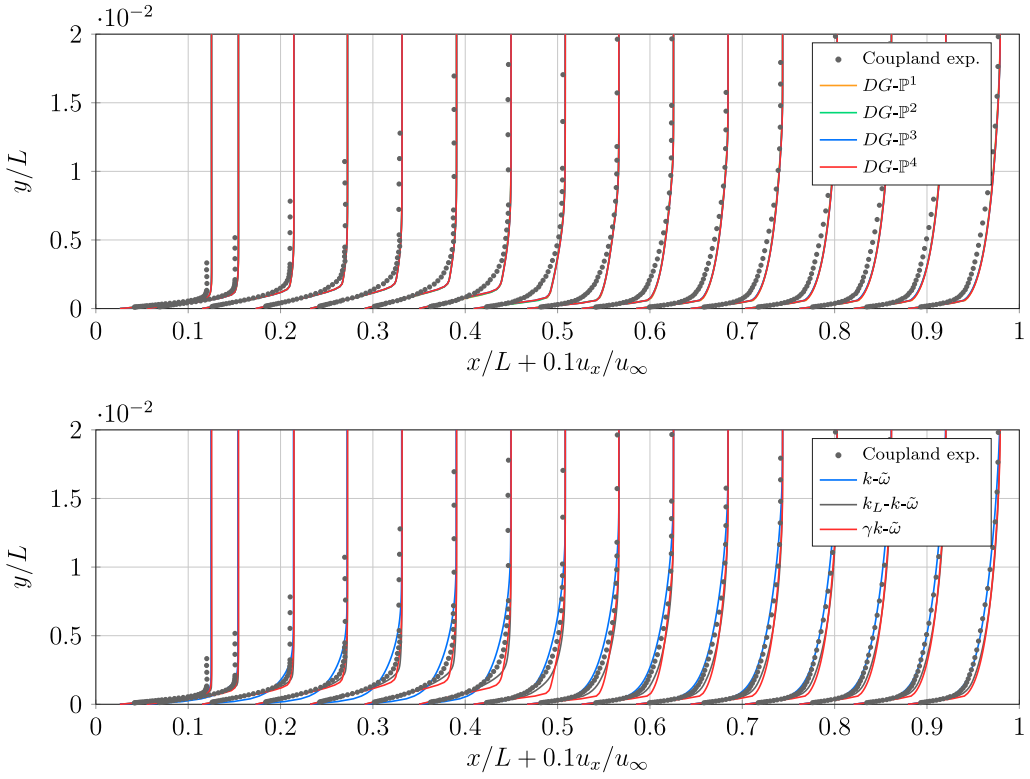

Fig. 9. Zero pressure gradient flat plates. x-component velocity at different locations x/L along the domain with the $\gamma k - \tilde{\omega}$ transition model, the $k - \tilde{\omega}$ turbulence model and the $k_L - k - \tilde{\omega}$ transition models [27,28] in the T3A case, from $\mathbb{P}^1$ to $\mathbb{P}^4$ solution approximation.

coefficient distribution near the transition is over-predicted, although the transition location is well predicted. Overall the results of the $\gamma k - \tilde{\omega}$ model show a better prediction of the transition in comparison to Holman et al. [8,9] in every case. In particular, the model of Holman et al. [8,9] predicted transition onset more accurately while transition length is captured better with the proposed model in T3A and T3A- cases.

Also the SA-BCM model demonstrates to be able to well predict the transition location in each case, although with different values of the freestream working variable $\tilde{\nu}_\infty$. In fact, the more accurate solution in comparison with experiments is given by $\tilde{\nu}_\infty/\nu = 1.5 \times 10^{-2}$ in the T3A case and $\tilde{\nu}_\infty/\nu = 1.5 \times 10^{-1}$ in the T3B case, where the turbulent intensity is moderate and high (3% and 6% respectively), while is given by $\tilde{\nu}_\infty/\nu = 1.5 \times 10^{-14}$ in the T3A- case, where the turbulent intensity is very low (0.9%). The values for the former cases are similar of the recommendation by Cakmakcioglu et al. [13,14], while for the latter case the value must be decreased to a very low value. The motivation of this value can be found in the very low level of the turbulent intensity, which allows to get closer to a natural transition mode case. Fig. 7 shows also the skin friction coefficient distribution in the T3A- case with the recommended value $\tilde{\nu}_\infty/\nu = 1.5 \times 10^{-2}$ to demonstrate the wrong prediction of the transition location and the skin friction's level of the fully turbulent boundary layer.

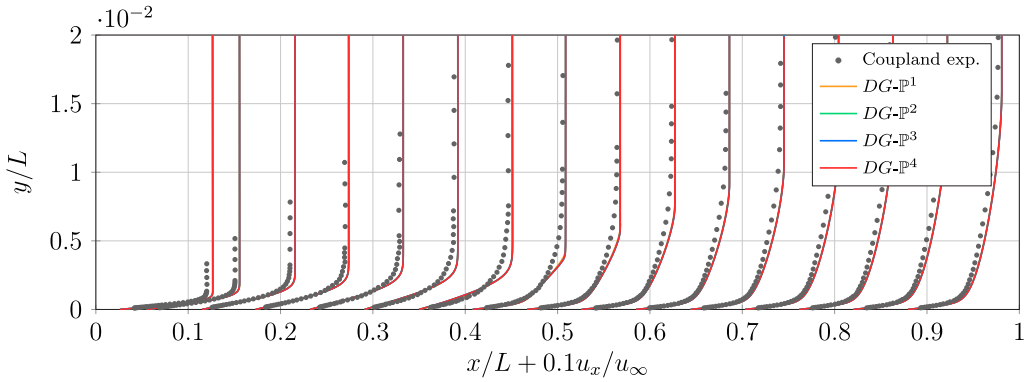

Fig. 10. Zero pressure gradient flat plates. x-component velocity at different locations x/L along the domain with the SA-BCM transition model and $\tilde{\nu}_\infty/\nu = 1.5 \times 10^{-2}$ in the T3A case, from $\mathbb{P}^1$ to $\mathbb{P}^4$ solution approximation.

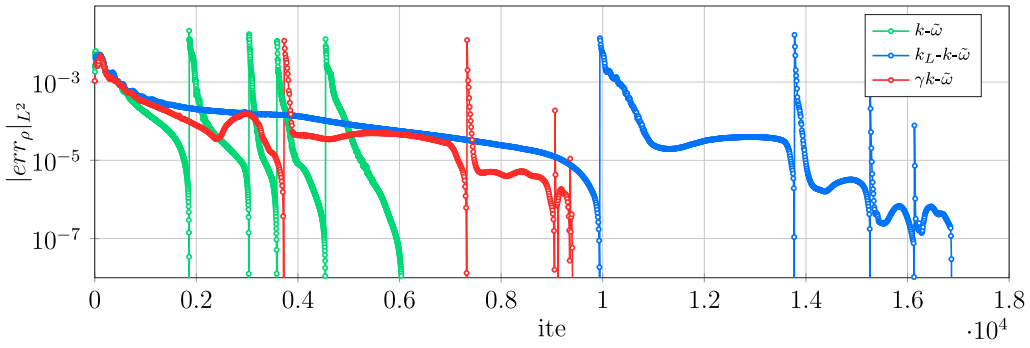

Fig. 11. Zero pressure gradient flat plates. The convergence history, in terms of the L^2 norm of the density residuals, of the $\gamma k - \tilde{\omega}$ transition model, the $k - \tilde{\omega}$ turbulence model [35] and the $k_L - k - \tilde{\omega}$ transition model [27,28] in the T3A case,from $\mathbb{P}^0$ to $\mathbb{P}^4$ solution approximation. In order to have a easy comparison symbols represent 1 iteration of 5, for $k - \tilde{\omega}$, and of 10, for the transition models.

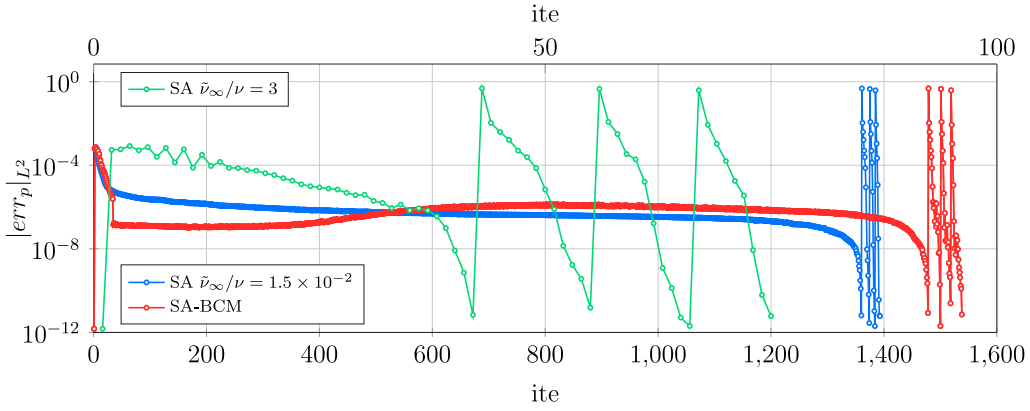

Fig. 12. Zero pressure gradient flat plates. The convergence history, in terms of the L^2 norm of the pressure residuals, of the SA-BCM transition model and $\tilde{\nu}_\infty/\nu = 1.5 \times 10^{-2}$ and the SA turbulence model [4] in the T3A case, from $\mathbb{P}^1$ to $\mathbb{P}^4$ solution approximation. The results with the SA turbulence model are reported with the prescribed value $\tilde{\nu}_\infty/\nu = 3$ [4] and the same value of the transition model $\tilde{\nu}_\infty/\nu = 1.5 \times 10^{-2}$ of the freestream working variable.

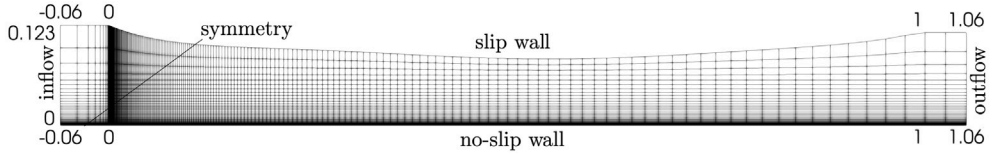

Fig. 13. Non-zero pressure gradient flat plates. Computational mesh of the T3C2, T3C3 and T3C5 cases. The boundary conditions in clockwise direction from the leading edge of the plate $(x, y) = (0, 0)$ are: symmetry, inflow, slip wall, outflow, and no-slip wall.

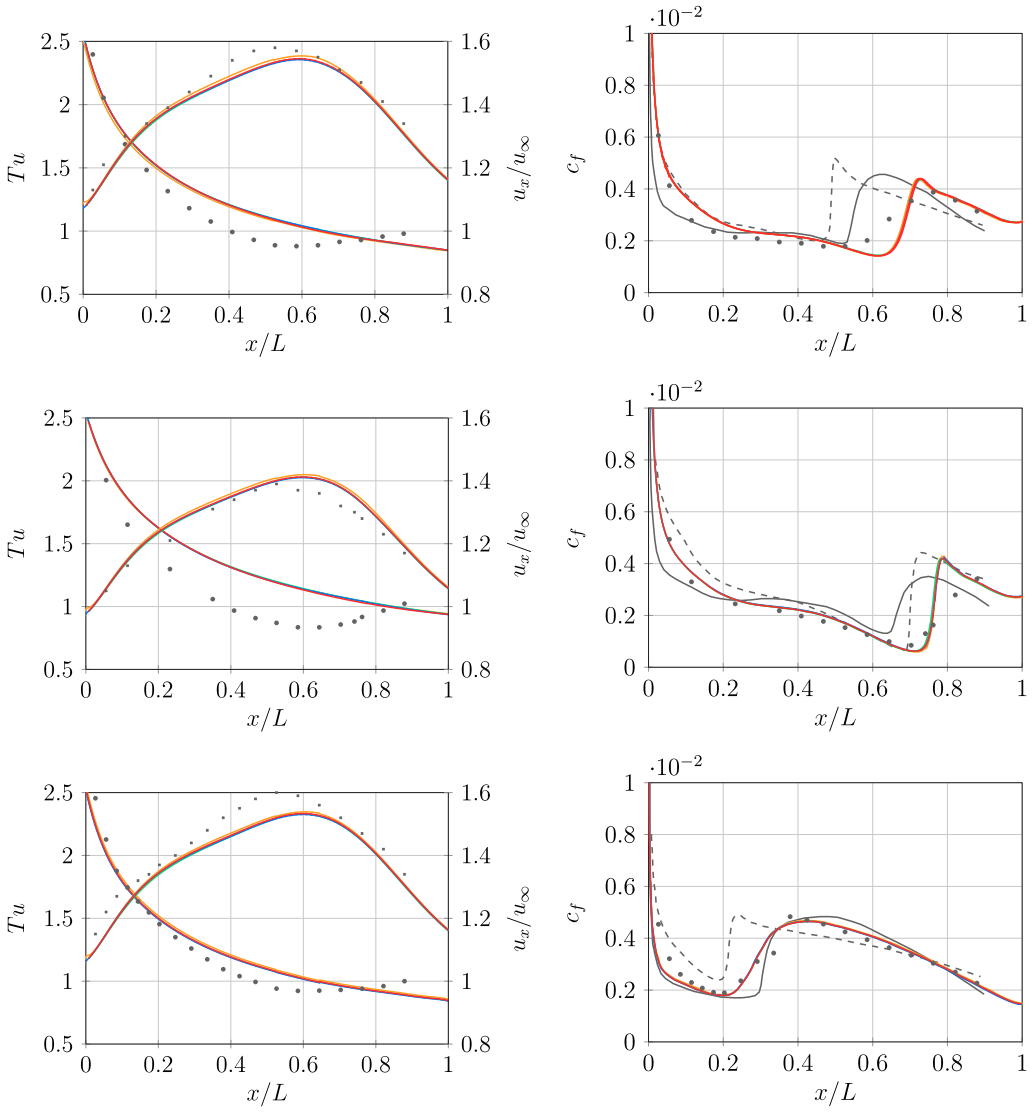

Fig. 14. Non-zero pressure gradient flat plates. Turbulent intensity Tu and x-component velocity u_x along the domain and skin friction coefficient c_f along the plate for the zero pressure gradient flat plates with the $\gamma k-\tilde{\omega}$ model, T3C2 (top), T3C3 and T3C5 (bottom), from $\mathbb{P}^1$ to $\mathbb{P}^4$ solution approximation. — $DG-\mathbb{P}^1$, — $DG-\mathbb{P}^2$, — $DG-\mathbb{P}^3$, — $DG-\mathbb{P}^4$, — Cakmakcioglu et al. SA-BC model, - - - Kubacki et al. $\gamma-\omega$ model, • Coupland exp.

In order to compare the performance of the models not only with the skin friction coefficient distributions, Fig. 8 shows the turbulent intensity profiles at different locations along the domain with the $\gamma k-\tilde{\omega}$ model, the $k-\tilde{\omega}$ turbulence model and the $k_L-k-\tilde{\omega}$ model [27,28] in the T3A case. For the Coupland experiments [18] only the x-component velocity fluctuations are here considered, i.e., $Tu=\sqrt{{u_x'}^2/3}/u_\infty$. While for the $k_L-k-\tilde{\omega}$ model [27,28] the turbulent intensity can be based both on the turbulent kinetic energy k, i.e., $Tu=\sqrt{2/3k}/u_\infty$, and the total kinetic energy $k_{TOT}=k+k_L$, i.e., $Tu=\sqrt{2/3k_{TOT}}/u_\infty$. The latter is able to model the kinetic energy also in the laminar and transitional boundary layers and for this reason guarantees an higher fidelity and a better agreement with experiments. While the turbulent intensity based only on the turbulent kinetic energy should represent the reference for the $\gamma k-\tilde{\omega}$ model, where only the turbulent kinetic energy is defined. The solution of the $\gamma k-\tilde{\omega}$ model underestimates the turbulent intensity in the laminar and transitional boundary layers, in comparison with the experiments and the numerical results of the $k_L-k-\tilde{\omega}$ model. Furthermore the turbulent kinetic energy of the $\gamma k-\tilde{\omega}$ model grows slower moving away from the wall.

Furthermore, Figs. 9 and 10 shows the x-component velocity profiles at different locations along the domain in the T3A case with the $\gamma k-\tilde{\omega}$ and the SA-BCM models, respectively, with different solution approximations in order to investigate more carefully the influence of the spatial accuracy on the solutions. Where, Fig. 9 shows also the solutions with the $k-\tilde{\omega}$ turbulence model and the $k_L-k-\tilde{\omega}$ model [27,28]. The solutions are overlapped between the transition models, i.e., the $\gamma k-\tilde{\omega}$, SA-BCM, and $k_L-k-\tilde{\omega}$ models, in the laminar and fully turbulent boundary layer, while the solution of the $\gamma k-\tilde{\omega}$ model guarantees a lower accuracy in the transitional boundary layer. As demonstrated also with the turbulent intensity profiles, the $\gamma k-\tilde{\omega}$ model suffers lower capabilities to reproduce each aspect of the transitional phenomena in comparison to a more comprehensive model. It is quite natural to conjecture that the $k_L-k-\tilde{\omega}$ model can model more aspects of the transitional mechanism. In fact, the $k_L-k-\tilde{\omega}$ model [27,28] is a phenomenological model with a transport equation also of the laminar contribution of the kinetic energy. In this model the turbulent kinetic energy is first due by the bypass transfer term, from the laminar kinetic energy transport equation, and after by the production term of its transport equation.

Finally, to assess the convergence behavior of both models, Figs. 11 and 12 show the convergence history of the $\gamma k-\tilde{\omega}$ model in comparison with the $k-\tilde{\omega}$ turbulence model [35], and the $k_L-k-\tilde{\omega}$ model [27,28], and of the SA-BCM model in comparison with the Spalart–Allmaras

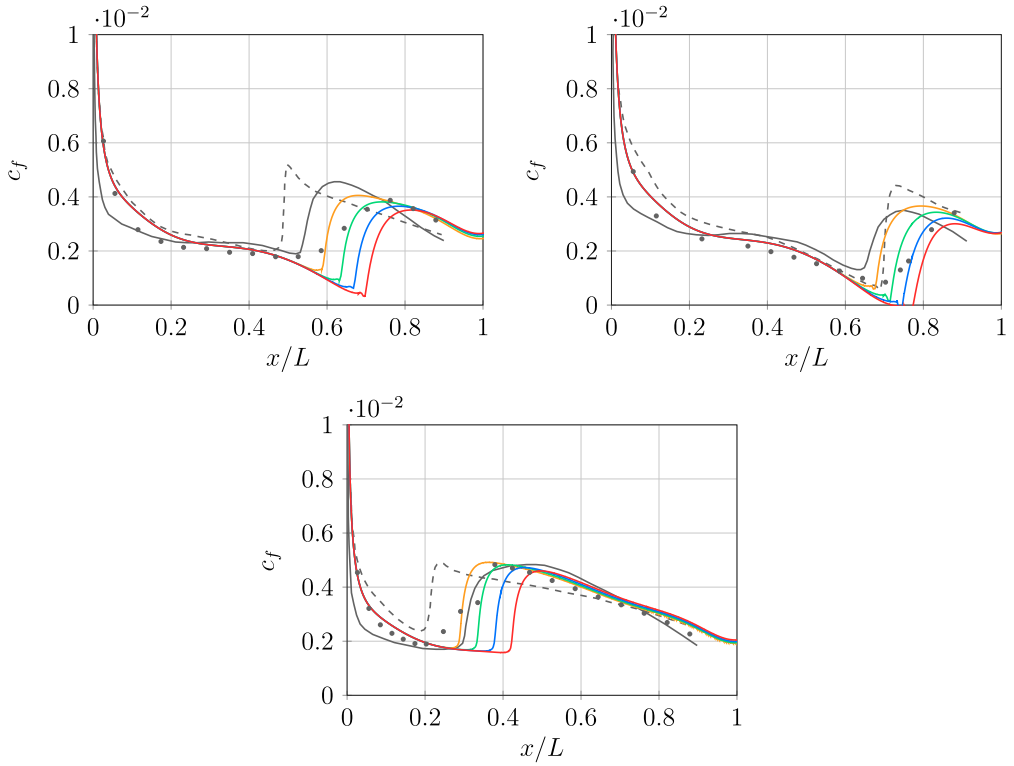

Fig. 15. Non-zero pressure gradient flat plates. Skin friction coefficient c_f along the plate for the zero pressure gradient flat plates with the SA-BCM model and different freestream working variables $\tilde{\nu}_\infty$, T3C2 (top, left), T3C3 (top, right) and T3C5 (bottom), $\mathbb{P}^4$ solution approximation. $\tilde{\nu}_\infty/\nu = 1.5 \times 10^{-1}$, $\tilde{\nu}_\infty/\nu = 1.5 \times 10^{-2}$, $\tilde{\nu}_\infty/\nu = 1.5 \times 10^{-3}$, $\tilde{\nu}_\infty/\nu = 1.5 \times 10^{-4}$, Cakmakcioglu et al. SA-BC model, Kubacki et al. $\gamma k - \omega$ model, Coupland exp.

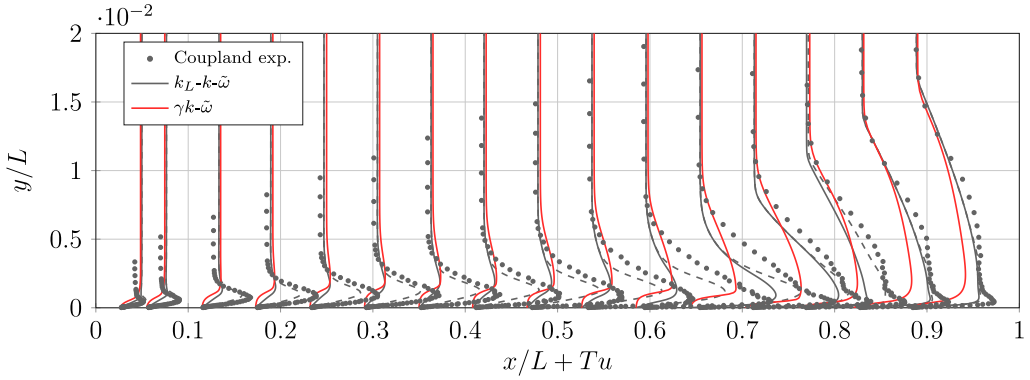

Fig. 16. Non-zero pressure gradient flat plates. Turbulent intensity $Tu = \sqrt{2/3k}/u_\infty$ at different locations x/L along the domain with the γk–$\tilde{\omega}$ model and the k_L–k–$\tilde{\omega}$ model [27,28] in the T3C2 case, $\mathbb{P}^4$ solution approximation. For the Coupland experiments [18] only the x-component velocity fluctuations are here considered, i.e., $Tu = \sqrt{\overline{u_x'^2}/3}/u_\infty$, in fact the y- and z-component are negligible. For the k_L–k–$\tilde{\omega}$ [27,28] transition model the dashed lines represent the turbulent intensity based on the total kinetic energy $Tu = \sqrt{2/3k_{TOT}}/u_\infty$ and $k_{TOT} = k + k_L$, while the solid lines the turbulent intensity based on the turbulent kinetic energy $Tu = \sqrt{2/3k}/u_\infty$.

turbulence model [4] in the T3A case, with the same "CFL law", e.g., $\text{CFL}_{\text{min}} = 1$, $\text{CFL}_{\text{max}} = 10^{20}$ and $\alpha = 1$. The results with the Spalart–Allmaras turbulence model are reported with the prescribed value $\tilde{\nu}_\infty/\nu = 3$ [4] and the same value of the transition model $\tilde{\nu}_\infty/\nu = 1.5 \times 10^{-2}$ of the freestream working variable to demonstrate that the higher number of iterations to reach the convergence can be ascribed mainly to the value of the boundary condition and not to the modifications of the transition model formulation.

5.2. Non-zero pressure gradient flat plates

The T3C2, T3C3 and T3C5 flat plates of the ERCOFTAC T3 series with non-zero pressure gradient are here used to validate and calibrate the transition models with bypass transition under a continuous variation of the pressure gradient, representing an aft-loaded turbine blade. They are characterized by different values of the freestream velocity u_∞ and the same value of the turbulence intensity at the leading edge of the plate Tu_{LE} (see Table 4). The freestream turbulent quantities of the $\gamma k - \tilde{\omega}$ model, e.g., Tu_∞ and $(\mu_T/\mu)_\infty$, are chosen in order to match the experimental turbulent intensity at the leading edge of the plate and the decay of the turbulent intensity along the domain. The same mesh, made of $n_e = 10\,600$ quadrilateral elements, is used for all the testcases, where the inflow boundary is set at $x/L = -0.06$ from the leading edge of the plate and adiabatic no-slip wall boundary condition is set on the plate (see Fig. 13). The mesh has $n_x = 200$ number of element in x-direction on the wall, i.e., $x/L > 0$, $n_y = 50$ number of element

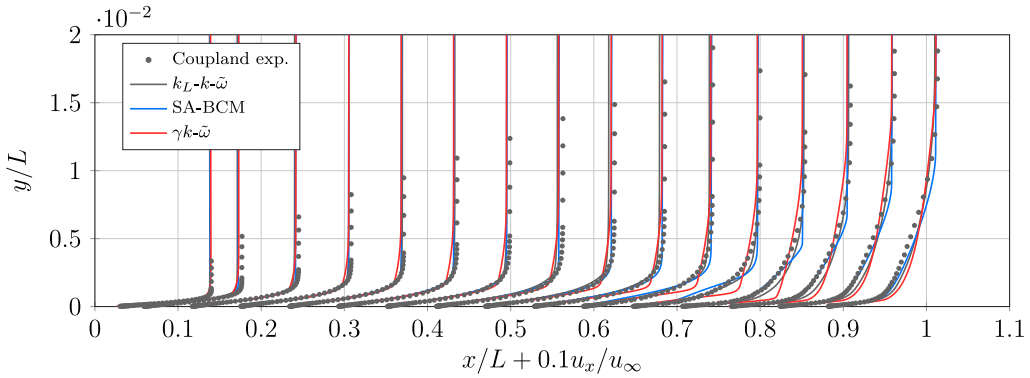

Fig. 17. Non-zero pressure gradient flat plates. x-component velocity at different locations x/L along the domain with the SA-BCM model and $\tilde{\nu}_\infty/\nu = 1.5 \times 10^{-2}$, the $\gamma k - \tilde{\omega}$ model, and the $k_L - k - \tilde{\omega}$ model [27,28] in the T3C2 case, $\mathbb{P}^4$ solution approximation.

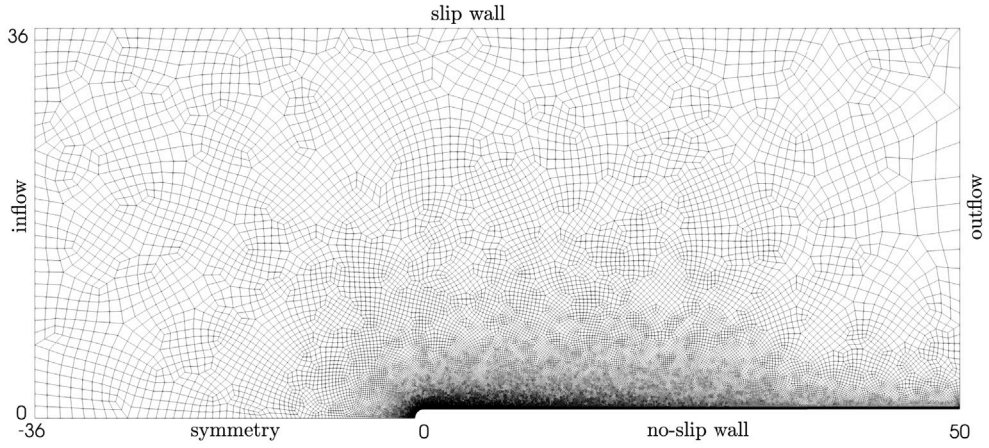

Fig. 18. Rounded leading edge flat plates. Computational mesh of the T3L cases. The boundary conditions in clockwise direction from the leading edge of the plate $(x, y) = (0, 0)$ are: symmetry, inflow, slip wall (or freestream), outflow, and no-slip wall. The mesh is here showed with linear edges.

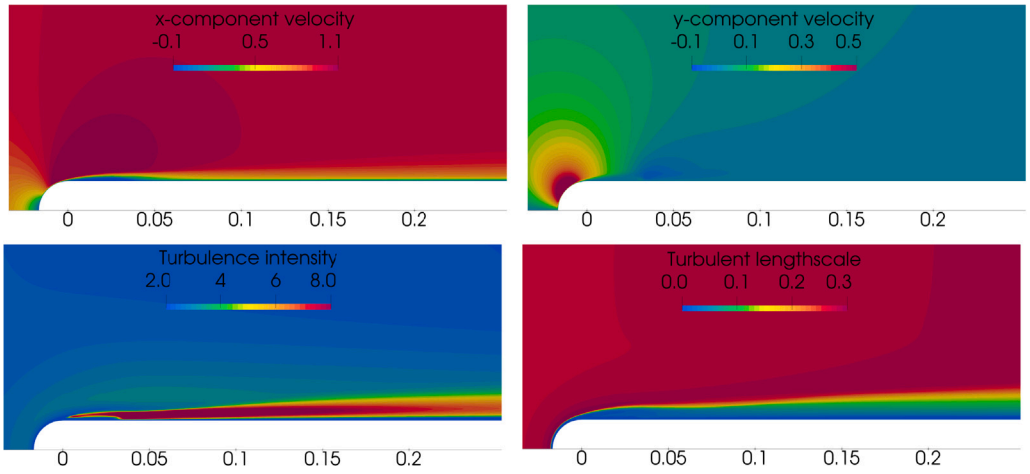

Fig. 19. Rounded leading edge flat plates. Contours of the x- and y-component velocity, the turbulent intensity $\sqrt{2/3k}/u_\infty$ and the turbulent lengthscale $\sqrt{k}/e^{\tilde{\omega}}$, with the $\gamma k - \tilde{\omega}$ model in the T3L3 case, $\mathbb{P}^4$ solution approximation.

in y-direction, and $\Delta y_1/L = \Delta x_1/L = 0.00005$ as height and length of the first element from the wall and from the leading edge of the plate in x-direction, respectively. The end-wall, with a slip wall boundary condition, and the height h/L allows to match the experimental x-component velocity distribution and the pressure gradient along the plate outside of the boundary layer. In particular, h/L is defined as

$$\frac{h}{L} = 3.845\left(\frac{x}{L}\right)^6 - 12.32\left(\frac{x}{L}\right)^5 + 15.198\left(\frac{x}{L}\right)^4 - 8.973\left(\frac{x}{L}\right)^3 + 2.659\left(\frac{x}{L}\right)^2 - 0.418\left(\frac{x}{L}\right) + 0.123.$$

At the end of the shaped slip end-wall, i.e., $x/L > 1$, an horizontal wall is set until $x/L = 1.06$ in order to improve the robustness of the convergence. The results of the proposed models are compared with the available experimental data of Coupland [18] and the numerical solution of the $\gamma k - \omega$ model of Kubacki et al. [10–12], and the SA-BCM model of Cakmakcioglu et al. [13,14].

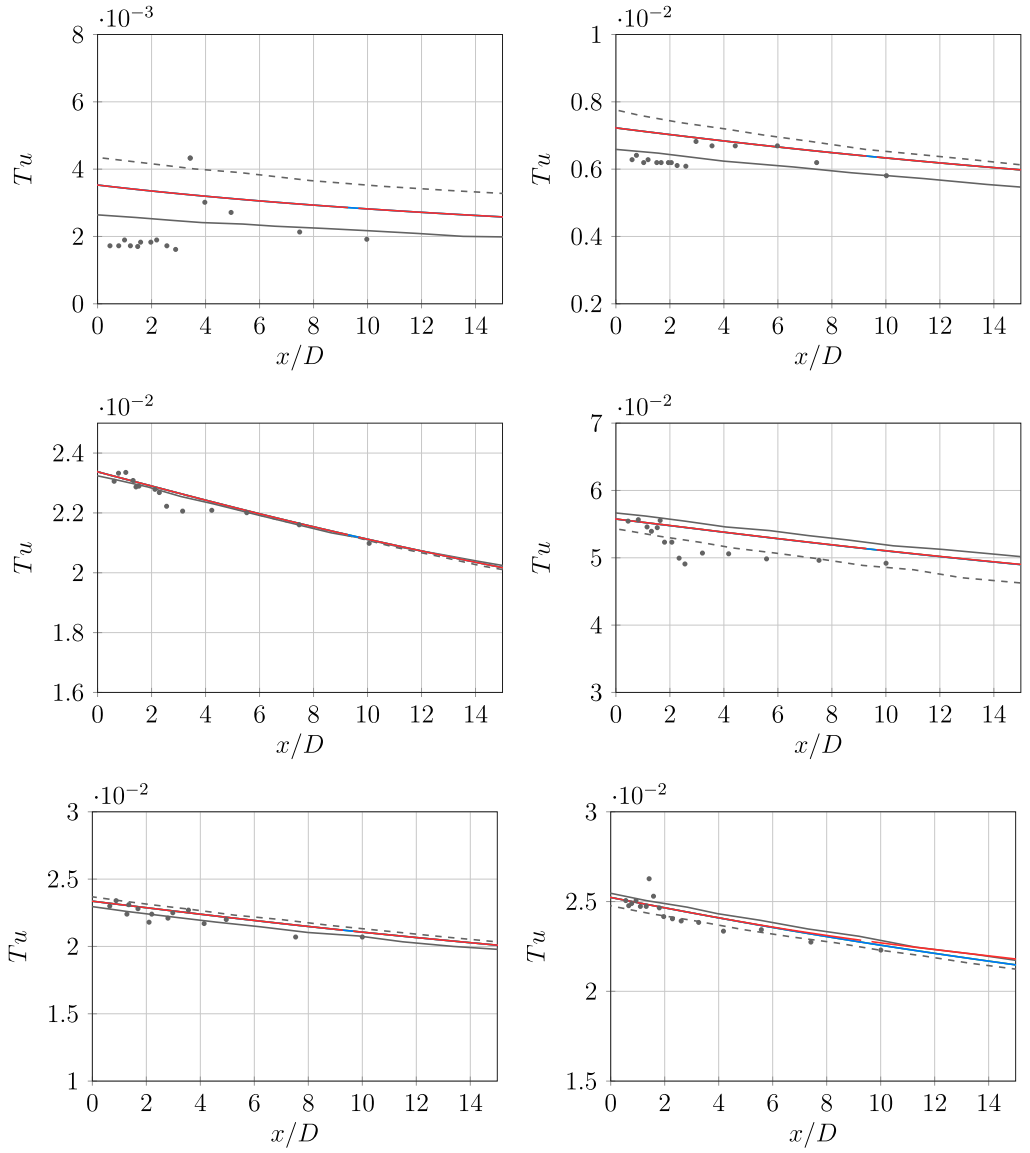

Fig. 20. Rounded leading edge flat plates. Turbulent intensity Tu along the domain for the rounded leading edge flat plates, from T3L1 (top, right) to T3L6 (bottom, left) with the $\gamma k - \tilde{\omega}$ model, from $\mathbb{P}^1$ to $\mathbb{P}^4$ solution approximation. The references from Vlahostergios et al. [36] are here reported with linear, solid lines, and non-linear, dashed lines, $k_L - k - \omega$ model. — $DG - \mathbb{P}^1$, — $DG - \mathbb{P}^2$, — $DG - \mathbb{P}^3$, — $DG - \mathbb{P}^4$, — Vlahostergios et al. $k_L - k - \omega$ model, • Coupland and Brierley exp.

Table 4
Non-zero pressure gradient flat plates. Flow conditions for the T3C2, T3C3 and T3C5 flat plates [18].

	T3C2	T3C3	T3C5
u_∞ [m/s]	5.0	3.7	8.4
Tu_{LE} [%]	3.0	3.0	3.0

Fig. 14 shows the skin friction coefficient distributions on the plate with the $\gamma k - \tilde{\omega}$ model and different solution approximations. Furthermore, Fig. 14 shows also the decay of the turbulent intensity and the x-component velocity along the domain outside of the boundary layer in order to prove the correctness of the boundary conditions of the turbulent quantities. Fig. 15 shows the skin friction coefficient distributions on the plate with the SA-BCM model and different values of the freestream working variable $\tilde{\nu}_\infty/\nu = 1.5 \times 10^i$ with $i = \{-1, \dots, -4\}$. The skin friction coefficient distributions of the $\gamma k - \tilde{\omega}$ model are almost overlapped with experiments in all the cases, where the transition flow region is shorter than in the experiments in the T3C2 and T3C3 cases. Starting from $\mathbb{P}^2$ approximation, the solution does not show significant difference increasing the accuracy, as spotlighted also in the previous cases. Overall, the results show a better prediction of the transition in comparison to Kubacki et al. [9–12] and Cakmakcioglu et al. [13,14] in every case. Also the SA-BCM model demonstrates to be able to well predict the transition location in each case, with slightly different values of the freestream working variable $\tilde{\nu}_\infty$. In fact, the more accurate solution in comparison with experiments is given by $\tilde{\nu}_\infty/\nu = 1.5{\times}10^{-2}$ in the T3C2 case, $\tilde{\nu}_\infty/\nu = 1.5{\times}10^{-3}$ in the T3C3 case, and $\tilde{\nu}_\infty/\nu = 1.5{\times}10^{-2}$ in the T3C5 case. This confirms that, where the turbulent intensity is not too low, the values of $\tilde{\nu}_\infty/\nu$ are similar to the recommendation by Cakmakcioglu et al. [13,14].

In order to compare the performance of the models not only with the skin friction coefficient distributions, Fig. 16 shows the turbulent intensity profiles at different locations along the domain with the $\gamma k{-}\tilde{\omega}$ model and the $k_L - k - \tilde{\omega}$ model [27,28], and Fig. 17 the x-component velocity profiles at different locations along the domain with the $\gamma k{-}\tilde{\omega}$, the SA-BCM models, and the $k_L - k - \tilde{\omega}$ model [27,28] in the T3C2 case. For the Coupland experiments [18] only the x-component velocity fluctuations are here considered, i.e., $Tu = \sqrt{u_x'^2/3}/u_\infty$. While for the $k_L - k - \tilde{\omega}$ model [27,28] the turbulent intensity can be based both

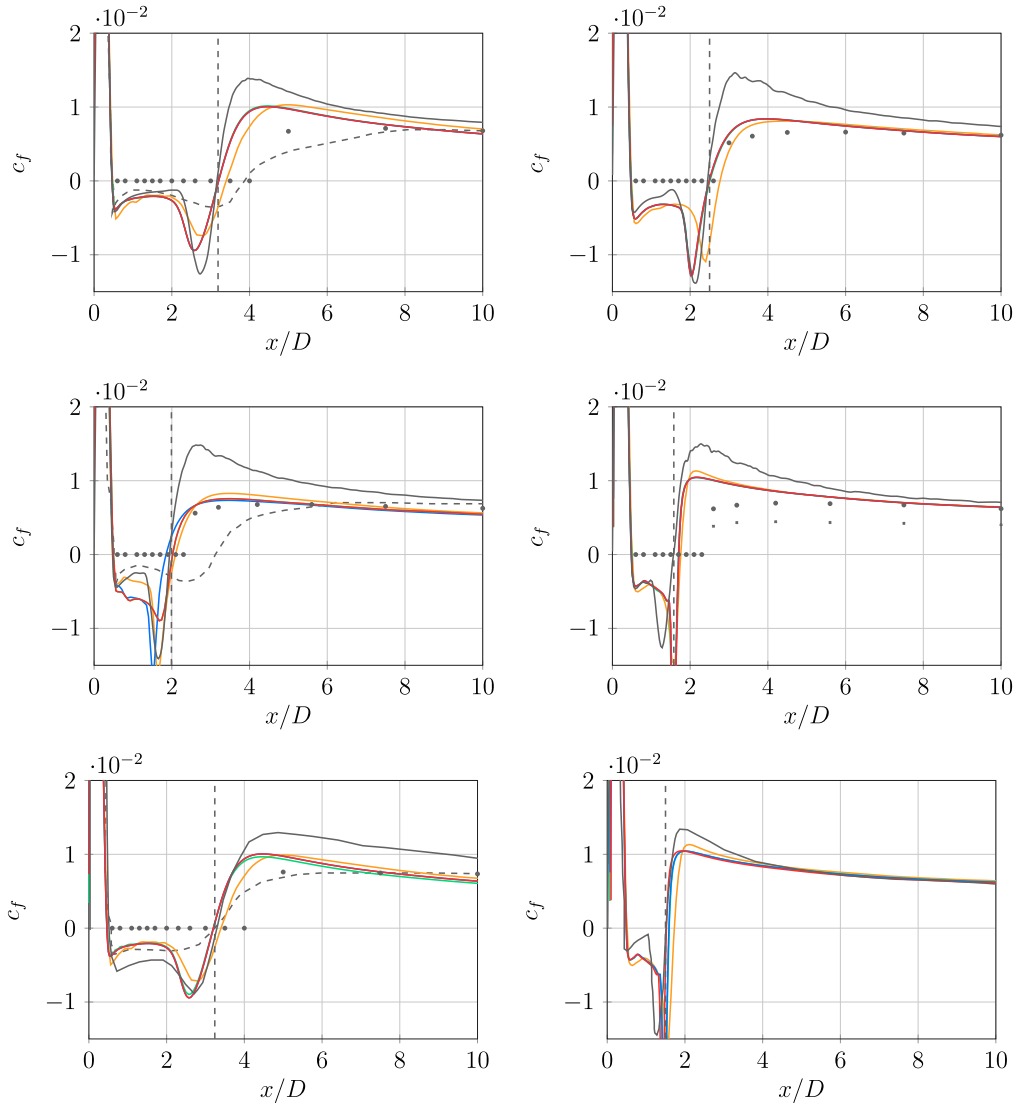

Fig. 21. Rounded leading edge flat plates. Skin friction coefficient c_f along the domain for the rounded leading edge flat plates, from T3L1 (top, right) to T3L6 (bottom, left) with the $\gamma k - \tilde{\omega}$ model, from $\mathbb{P}^1$ to $\mathbb{P}^4$ solution approximation. The vertical dashed line represent the experimental length of the laminar separation bubble [19]. The reference from Vlahostergios et al. [36] are here reported with linear $k_L - k - \omega$ model. In the T3L4 case both the experimental data, calculated (dots) and modeled (crosses), are reported. — $DG - \mathbb{P}^1$, — $DG - \mathbb{P}^2$, — $DG - \mathbb{P}^3$, — $DG - \mathbb{P}^4$, - - - Vlahostergios et al. $k_L - k - \omega$ model, — Bassi et al. ILES, • Coupland and Brierley exp.

on the turbulent kinetic energy k, i.e., $Tu = \sqrt{2/3k}/u_\infty$, and the total kinetic energy $k_{TOT} = k + k_L$, i.e., $Tu = \sqrt{2/3k_{TOT}}/u_\infty$. Similarly to the previous cases, i.e., T3A, T3B and T3A-, the turbulent kinetic energy of the $\gamma k - \tilde{\omega}$ model grows slower moving away from the wall, in comparison with the experiments and the numerical results of the $k_L - k - \tilde{\omega}$ model. Also the x-component velocity profiles shows the same differences of the previous cases between the $k_L - k - \tilde{\omega}$, $\gamma k - \tilde{\omega}$, and SA-BCM models. In fact, the solutions are overlapped between the transition models in the laminar and fully turbulent boundary layer, while the solution of the $\gamma k - \tilde{\omega}$ model guarantees a lower accuracy in transitional boundary layer. Instead, the solutions of the SA-BCM model are in agreement with those of the $k_L - k - \tilde{\omega}$ model also in the transitional boundary layer.

5.3. Rounded leading edge flat plates

The T3L1–T3L6 rounded leading edge flat plates of the ERCOFTAC T3 series with zero pressure gradient are here used to validate and calibrate the transition models with separation-induced transition. They are characterized by different values of the freestream Reynolds number Re_∞ and turbulent intensity at the leading edge of the plate Tu_{LE}, ranging from 0.2% to 5.6% (see Table 5). The freestream turbulent quantities of the $\gamma k - \tilde{\omega}$ model, e.g., Tu_∞ and $(\mu_T/\mu)_\infty$, are chosen in order to match the experimental turbulent intensity at the leading edge and the decay of the turbulent intensity along the domain. In particular the following turbulent intensity and Reynolds numbers are considered: $Tu_{LE} = \{0.2\%, 0.65\%, 2.3\%, 5.6\%\}$ and $Re_\infty = \{3\,450, 1\,725, 6\,900\}$. The Reynolds number is based on the diameter of the leading edge of the plate D and the freestream flow conditions. The same mesh, made of $n_e = 15\,500$ quadrilateral elements with quadratic edges, is used for all the testcases, where the outflow boundary is set at $x/D = 50$ from the leading edge of the plate and adiabatic no-slip wall boundary condition is set on the plate (see Fig. 18). The mesh has 100 surface elements on the rounded leading edge and 600 on the flat plate, i.e., $n_x = 700$ number of elements in x-direction on the wall, and $\Delta y_1/D = 0.002$ as height of the first element from the wall. The results of the proposed models are compared with the available experimental data of Coupland and Brierley [19] and the numerical solution of Bassi et al. [37], with an high-fidelity implicit LES (ILES), and Vlahostergios et al. [36], with the linear and non-linear $k - k_L - \omega$ transition model.

Fig. 19 shows the contours of the x- and y-component velocity, the turbulent intensity $Tu = \sqrt{2/3k}/u_\infty$ and the turbulent length scale

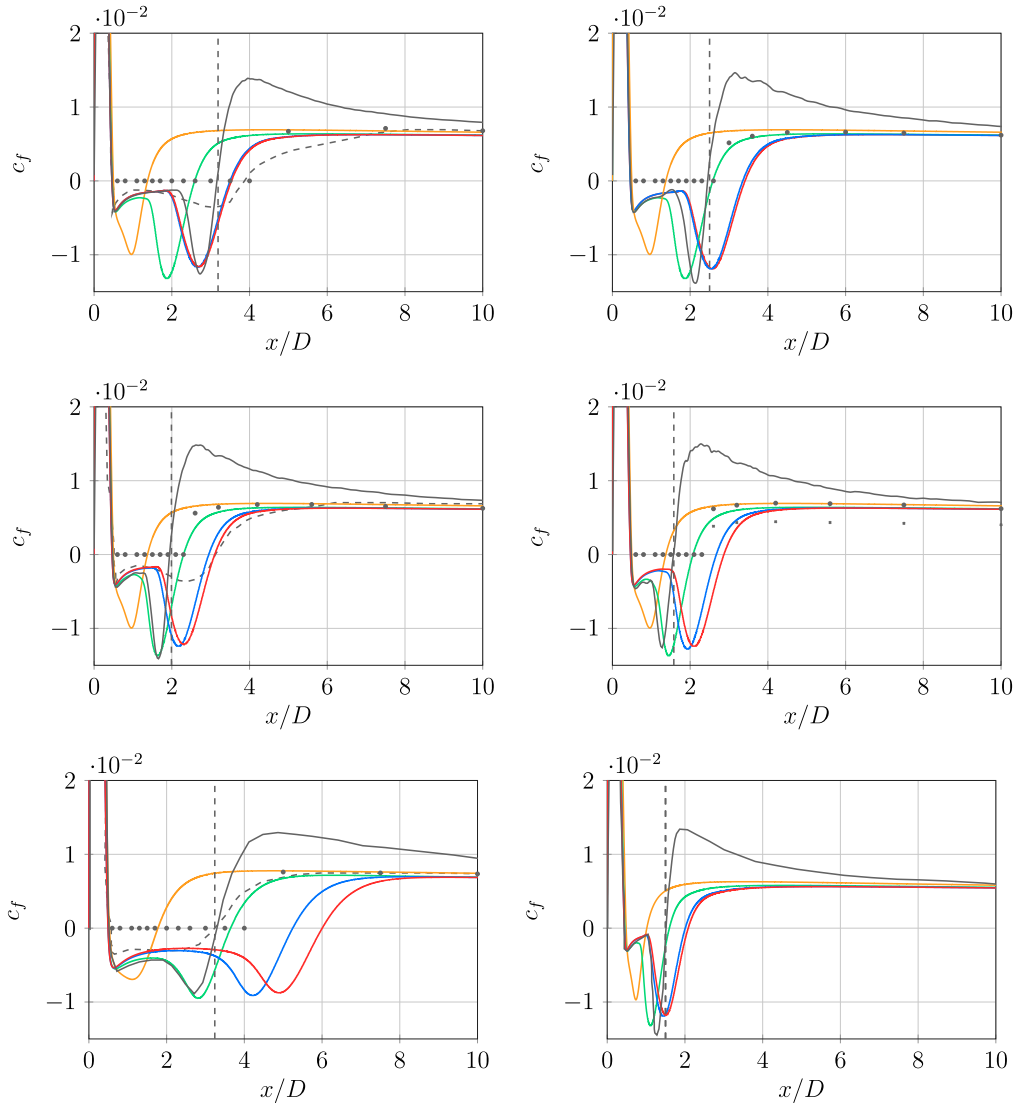

Fig. 22. Rounded leading edge flat plates. Skin friction coefficient c_f along the domain for the rounded leading edge flat plates with the SA-BCM model and different freestream working variables $\tilde{\nu}_\infty$, from T3L1 (top, right) to T3L6 (bottom, left), $\mathbb{P}^4$ solution approximation. The vertical dashed line represent the experimental length of the laminar separation bubble [19]. The reference from Vlahostergios et al. [36] are here reported with linear $k_L - k - \omega$ model. In the T3L4 case both the experimental data, calculated (dots) and modeled (crosses), are reported. — $\tilde{\nu}_\infty/\nu = 1.5 \times 10^1$, — $\tilde{\nu}_\infty/\nu = 1.5 \times 10^0$, — $\tilde{\nu}_\infty/\nu = 1.5 \times 10^{-1}$, — $\tilde{\nu}_\infty/\nu = 1.5 \times 10^{-2}$, - - - Vlahostergios et al. $k_L - k - \omega$ model, —— Bassi et al. ILES, • Coupland and Brierley exp.

Table 5
Rounded leading edge flat plates. Flow conditions (top) and length of the laminar separation bubble l/D as a function of the freestream Reynolds number Re_∞ and the turbulent intensity at the leading edge of the plate Tu_{LE} (bottom). The lengths of the laminar separation bubble of the SA-BCM model are here reported with the best values of the freestream working variables, e.g., $\tilde{\nu}_\infty/\nu = 1.5 \times 10^{-2}$, 1.5×10^0, 1.5×10^0, 1.5×10^0, 1.5×10^0 and 1.5×10^0 respectively in the different cases.

	T3L1	T3L2	T3L3	T3L4	T3L5	T3L6
Re_∞ [–]	3450	3450	3450	3450	1725	6900
Tu_{LE} [%]	0.20	0.65	2.30	5.60	2.30	2.30
Bassi et al. ILES [37]	2.69	2.00	1.49	1.08	2.74	1.00
$\gamma k - \tilde{\omega}$ model	2.70	2.00	1.51	1.16	2.74	1.00
SA-BCM model	2.89	2.08	1.61	1.44	2.82	1.03

$\lambda_T = \sqrt{k}/e^{\tilde{\omega}}$, with the $\gamma k - \tilde{\omega}$ model in the T3L3 case. Evans [38] and Holland and Evans [39] spotlighted that the unsteadiness in turbulent boundary layers results in higher time-averaged boundary layer integral parameters. After the reattachment the boundary layer increases the velocity fluctuations and the momentum loss with a local increment also of the skin friction coefficient. For this reason, in the results here reported, the (steady) transition models should underestimate the distribution of the skin friction coefficient in comparison with the (unsteady) ILES by Bassi et al. [37] after the reattachment of the boundary layer, due to a natural inability to predict the velocity fluctuations of steady simulations and the averaged formulation of the RANS equations. Probably due to probe position, sampling frequency, and time-averaged issues of the measurements also the experiments of Coupland and Brierley [19] suffer from inaccuracy in the reattachment flow region downstream of the bubble, where the unsteadiness of the boundary layer is higher.

Fig. 20 shows the decay of the turbulent intensity along the domain outside of the boundary layer with the $\gamma k - \tilde{\omega}$ model in all the cases in order to prove the correctness of the boundary conditions of the turbulent quantities. While Figs. 21 and 22 show the skin friction coefficient distributions on the plate in all the cases with the $\gamma k - \tilde{\omega}$ model and the SA-BCM model, respectively. Fig. 21 shows the solutions of the $\gamma k - \tilde{\omega}$ model with different solution approximations, while Fig. 22 shows the solutions of the SA-BCM model with different values of the freestream working variable $\tilde{\nu}_\infty/\nu = 1.5 \times 10^i$ with $i = \{1, \dots, -2\}$.

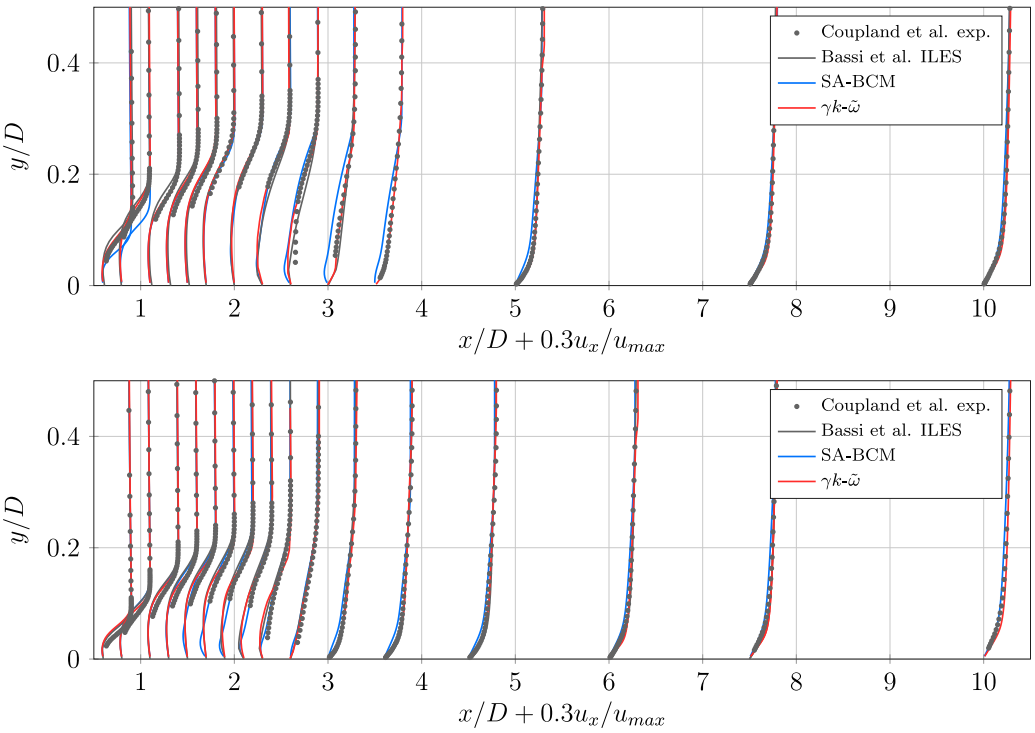

Fig. 23. Rounded leading edge flat plates. x-component velocity u_x/u_{max} at different locations x/D along the domain in the T3L1 (top) and T3L2 (bottom) case, with the $\gamma k-\tilde{\omega}$ and SA-BCM models, $\mathbb{P}^4$ solution approximation. The results with the SA-BCM model are here reported with the best values of the freestream working variables, e.g., $\tilde{\nu}_\infty/\nu = 1.5\times10^{-2}$ and 1.5×10^{0} in the T3L1 and T3L2 case, respectively.

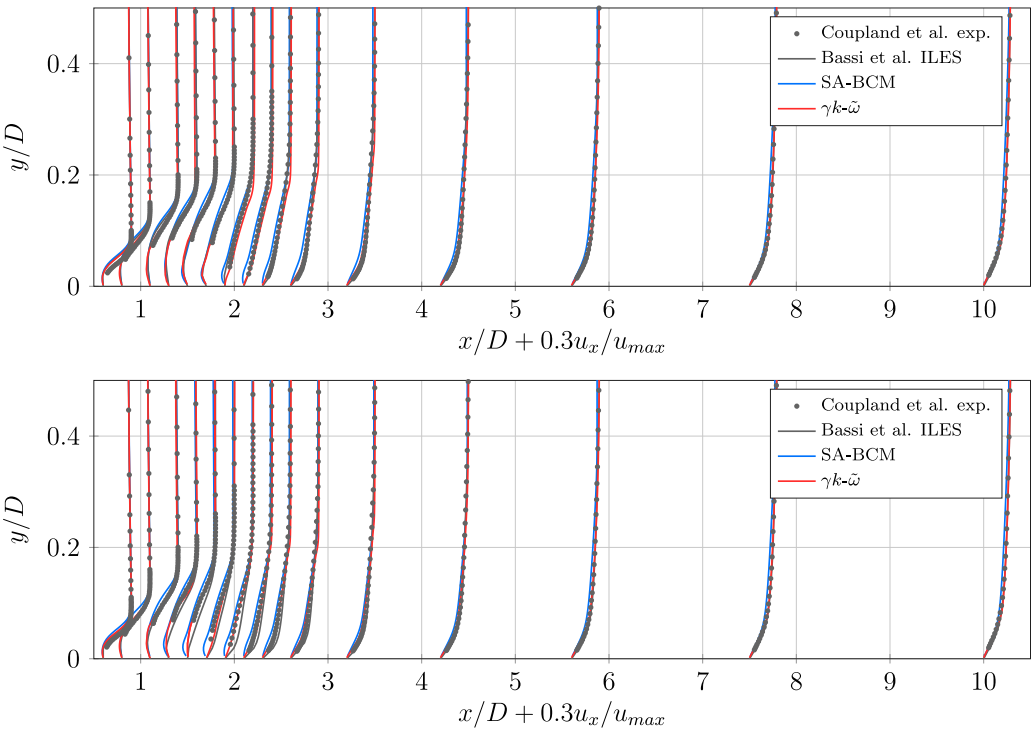

Fig. 24. Rounded leading edge flat plates. x-component velocity u_x/u_{max} at different locations x/D along the domain in the T3L3 (top) and T3L4 (bottom) case, with the $\gamma k-\tilde{\omega}$ and SA-BCM models, $\mathbb{P}^4$ solution approximation. The results with the SA-BCM model are here reported with the best values of the freestream working variables, e.g., $\tilde{\nu}_\infty/\nu = 1.5\times10^{0}$ and 1.5×10^{0} in the T3L3 and T3L4 case, respectively.

Regarding the $\gamma k-\tilde{\omega}$ model the solutions of the skin friction coefficient are almost overlapped with experiments in all the cases, where starting from $\mathbb{P}^2$ approximation the solution has no significant difference increasing the accuracy. The results show a better prediction of the transition in comparison to Vlahostergios et al. [36] in every case. In particular the main discrepancy of the results of the $\gamma k-\tilde{\omega}$ model is in the intensity of the skin friction coefficient in the reattached and fully turbulent boundary layer, in fact these values are in agreement

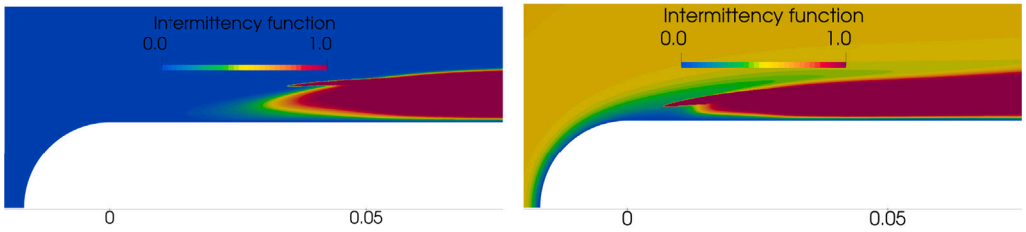

Fig. 25. Rounded leading edge flat plates. Contours of the γ_{BC} intermittency function of the SA-BCM model in the T3L1 (right) and T3L3 (left) case, $\mathbb{P}^4$ solution approximation.

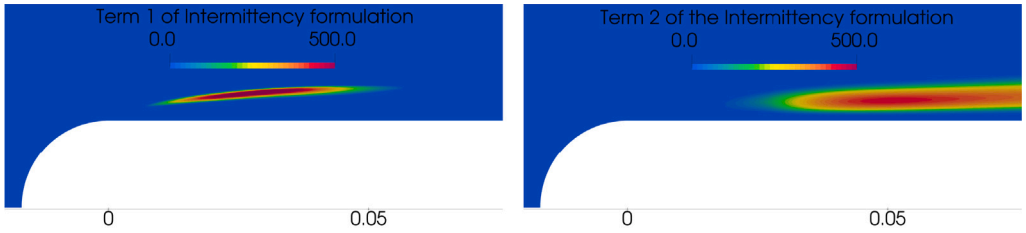

Fig. 26. Rounded leading edge flat plates. Contours of the $Term_1$ (left) and $Term_2$ (right) of the intermittency function formulation γ_{BC} of the SA-BCM model in the T3L3 case, $\mathbb{P}^4$ solution approximation.

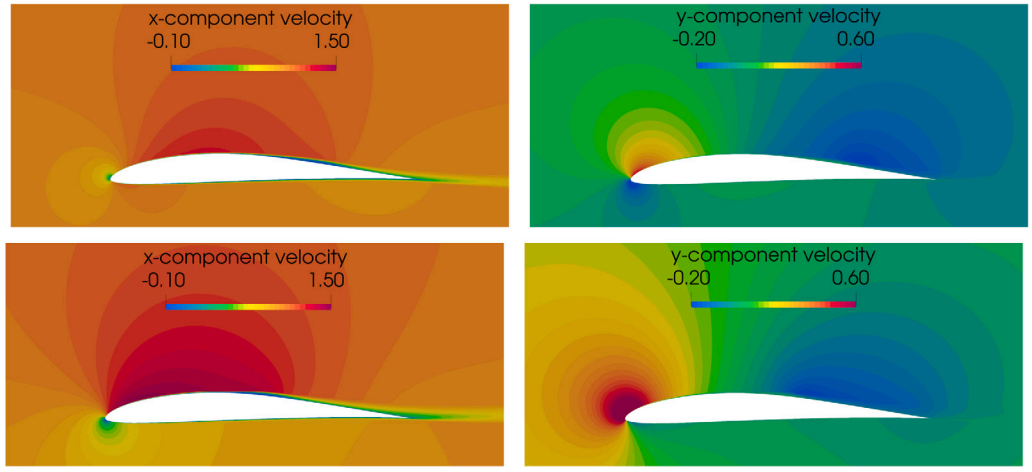

Fig. 27. Eppler E387 Airfoil. Contours of the x- and y-component velocity with the SA-BCM model and $\tilde{\nu}_\infty/\nu = 1.5\times10^{-2}$ in the case with 0° (top) and 6° (bottom) angle of attack, $\mathbb{P}^4$ solution approximation.

with experiments and the numerical results of Vlahostergios et al. [36], while underestimates the numerical results of Bassi et al. [37]. In fact, as previously described, the higher skin friction coefficient distribution of the high-fidelity simulations is due the unsteadiness of the flow and in particular the velocity fluctuations.

Also the SA-BCM model demonstrates to be able to well predict the transition and reattachment location in each case, although with different values of the freestream working variable $\tilde{\nu}_\infty$. In fact, the more accurate solution in comparison with experiments is given with $\tilde{\nu}_\infty/\nu = 1.5\times10^{-2}$, 1.5×10^{0}, 1.5×10^{0}, 1.5×10^{0}, 1.5×10^{0} and 1.5×10^{0} respectively in all the cases. Also on this testsuite, as in the T3A- case, lower levels of the turbulent intensity need lower values of the freestream working variable $\tilde{\nu}_\infty$ for the SA-BCM model. In fact, in the T3L1 case the more accurate solution is with the lower value of the freestream working variable value, i.e., $\tilde{\nu}_\infty/\nu = 1.5\times10^{-2}$. In comparison with the natural transition mode cases the freestream working variable has a lower influence on the performance of the SA-BCM model and the solutions with different values of $\tilde{\nu}_\infty$ are more similar with higher Reynolds numbers and turbulent intensities.

Figs. 23 and 24 show the x-component velocity profiles at different locations along the domain in the cases from T3L1 to T3L4, with the $\gamma k-\tilde{\omega}$ and the SA-BCM models. The solutions of the models are in agreement both with the experiments and the high-fidelity ILES by Bassi et al. [37]. Only negligible differences can be noticed in the location of the reattachment of the shear layer on the plate between the solutions with the $\gamma k-\tilde{\omega}$ model and the references. In fact, the x-component velocity gradient in wall-normal direction is higher in the ILES solution [37] in those regions, confirming also the higher values in the distribution of the skin friction coefficients. While the solutions of the SA-BCM model underestimate the height of the bubble near the leading edge of the plate in the T3L1 case.

Fig. 25 shows the contours of the intermittency function γ_{BC} of the SA-BCM model in the T3L1 and T3L3 cases, while Fig. 26 shows the $Term_1$ and $Term_2$ contributions of the intermittency function in the latter case. The intermittency function γ_{BC} can assume different values in the freestream, for example in the T3L1 case is $\sim$0 while in the T3L3 case $\sim$0.5. In fact, in the T3L3 case the value of the freestream working variable $\tilde{\nu}_\infty/\nu = 1.5\times10^{0}$ immediately activates the intermittency function, where the freestream γ_{BC} value is due to the $Term_2$ contribution. Indeed, it is possible that the χ_2 constant should be re-calibrated for such a large value of the freestream working variable, which was clearly not considered in [13,14].

For the $\gamma k-\tilde{\omega}$ the γ_2 and γ_3 formulations are closer to the wall after the reattachment of the boundary layer, in comparison with the

other formulations. In fact, these formulation are not based on distance from the wall and, furthermore, the γ_3 formulation is written with the dissipation rate which is high near wall. Instead, the γ_1, γ_2 and γ_4 formulations contain the turbulent kinetic energy which slows the growth of the intermittency moving in normal direction from the wall. $Term_2$ of γ_{BC}, and of γ_4, allows the production of the intermittency inside the boundary layer, even if this term has to follow the behavior of the turbulent kinetic energy and the SA's working variable, respectively in the $\gamma k - \tilde{\omega}$ and SA-BCM model, which are zero near wall.

5.4. Eppler387 airfoil

The last testsuite with separation-induced transition is the flow around an Eppler E387 airfoil, where the experiments by McGhee et al. [20] at Langley Low-Turbulence Pressure Tunnel (LTPT) are available in literature at different angles of attack. The freestream Reynolds number is $Re_\infty = 200\,000$, based on the freestream flow conditions and the chord of the airfoil, and the freestream turbulent intensity is $Tu_\infty = 0.1\%$. The freestream Mach number is $Ma_\infty = 0.1$ to consider the flow essentially incompressible. The freestream turbulent quantities of the $\gamma k - \tilde{\omega}$ model, e.g., Tu_∞ and $(\mu_T/\mu)_\infty$, are chosen in order to match the turbulent intensity at the leading edge of the airfoil. No information are available about the experimental decay of the turbulent kinetic energy along the domain. In order to compare different pressure gradient conditions different angles of attack are considered: $\alpha = \{0°, \dots, 10°\}$. The same mesh, made of $n_e = 2880$ quadrilateral elements with quadratic edges, is used for all the cases, where the freestream boundary is set at $100c$ from the airfoil and adiabatic no-slip wall boundary condition is set on the airfoil (see Fig. 28). The mesh has 60 surface elements on the airfoil and $\Delta y_1/D = 0.0002$ as height of the first element from the wall. The results of the proposed models are compared with the available experimental data of McGhee et al. [20] and the numerical solution of the SA-BCM model of Cakmakcioglu et al. [13,14]. Fig. 27 shows the contours of the x- and y-component velocity with the SA-BCM model and $\tilde{\nu}_\infty/\nu = 1.5\times10^{-2}$ in the case with 0° and 6° angle of attack.

Figs. 29 and 30 show the pressure coefficient distributions on the airfoil with the $\gamma k - \tilde{\omega}$ model, with different solution approximations, and the SA-BCM model, with different values of the freestream working variable $\tilde{\nu}_\infty/\nu = 1.5\times10^i$ with $i = \{0, \dots, -3\}$, respectively. The solutions of both the models, starting from $\mathbb{P}^2$ solution approximation for the $\gamma k - \tilde{\omega}$ model, are almost overlapped with the experiments. The $\gamma k - \tilde{\omega}$ model introduces serious difficulties in the convergence, in fact these cases need an higher number of iterations to convergence, probably due to the low turbulent intensity in a large domain with large elements near the freestream boundary.

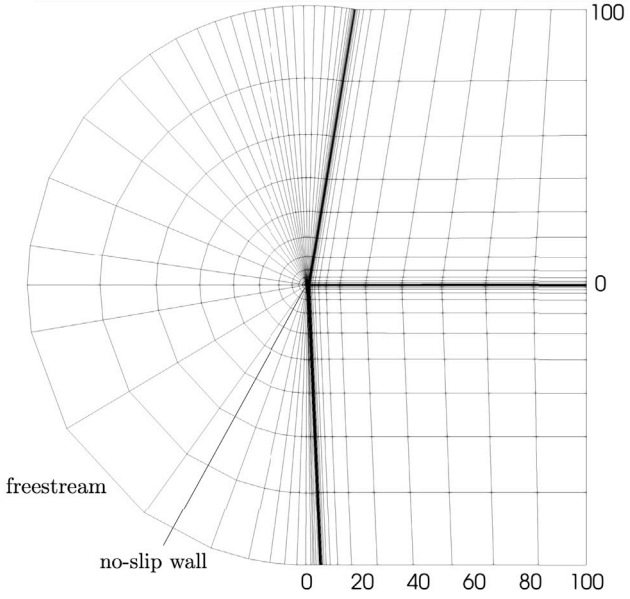

Fig. 28. Eppler E387 Airfoil. Computational mesh of the Eppler E387 cases. The boundary conditions are freestream on the outer boundary and no-slip on the airfoil. The mesh is here showed with linear edges.

In order to compare the performance of the models not only with the pressure coefficient distributions, Fig. 31 shows the lift c_l and drag c_d coefficient and the laminar separation (LS) and turbulent reattachment (TR) location with the $\gamma k - \tilde{\omega}$ and the SA-BCM model. Both the models are able to predict the transition, the separation and the reattachment of the flow at every angles of attack, where the SA-BCM model slight overestimate the bubble length for $\alpha < 7°$ and underestimate the bubble length for $\alpha > 7°$. With the higher angles of attack, e.g., $\alpha > 8°$, the separation takes place at the leading edge of the airfoil and the transition flow features are closed to those of the ERCOFTAC rounded leading-edge flat plates. In the experiments [20] between 7° and 8° the flow is attached and natural transition happens, whereas all the transition models from literature [40] show separation-induced transition. Also with the $\gamma k - \tilde{\omega}$ and the SA-BCM models a laminar separation and a turbulent reattachment of the flow can be noticed at this critical range of values of the angle of attack. Furthermore, while the transition location is sensitive to the model's prediction capabilities, the lift and drag coefficients are similar for both the models.

6. Conclusions

The implementation of a modified version of the $k - \tilde{\omega}$ [7] and Spalart–Allmaras [4] turbulence models in a high-order dG solver to predict bypass and separation-induced transition is here presented. The modifications of these turbulence models are based on the $\gamma k - \omega$ by Holman and Fürst [8,9] and Kubacki et al. [10–12], and the SA-BCM by Cakmakcioglu et al. [13,14].

Both the proposed transition models, e.g., the $\gamma k - \tilde{\omega}$ and SA-BCM model, are correlation-based algebraic models that rely on local and freestream flow information and include an intermittency function instead of an intermittency equation, and are validated on benchmark cases from the ERCOFTAC T3 suite to the Eppler 387 airfoil, with different transition mode, freestream Reynolds number and turbulent intensity, and pressure gradient. The accuracy of both the models is demonstrated in comparison with experiments and numerical results from literature with similar models [8–11,13,14,36], for increasing order of accuracy. A good choice of the freestream working variable for the SA-BCM model is mandatory. In particular cases with a low level of the freestream turbulent intensity need lower values of the working variable at the boundary, which are out of the prescribed range of values [13,14]. The work is in progress in the application of the models on more complex testcases, as turbine or compressor cascades, and in the coupling of the models with a p-multigrid algorithm [3].

CRediT authorship contribution statement

A. Crivellini: Conceptualization, Methodology, Validation, Formal analysis. **A. Ghidoni:** Resources, Supervision, Project administration. **G. Noventa:** Conceptualization, Methodology, Validation, Formal analysis, Data curation, Writing – original draft, Writing – review & editing, Visualization.

Declaration of competing interest

The authors declare that they have no known competing financial interests or personal relationships that could have appeared to influence the work reported in this paper.

Data availability

Data will be made available on request.

Appendix. Mesh sensitivity

To validate the implementation of both the transition models, a spatial sensitivity analysis is carried out for on T3A test case. Three different meshes with 2400 (coarse), 8800 (medium) and 33 600 (fine) quadrilateral elements, are used, where the inlet boundary is set at $x/L = -0.06$ from the leading edge of the plate and adiabatic no-slip wall boundary condition is set on the plate. The medium mesh is the same used in Section 5.1 for the comparison of the prediction capabilities of the models. The same solution approximations are used on all the meshes, where Table A.6 shows the details and the degrees of freedom (DoFs) of the different meshes and solution approximations.

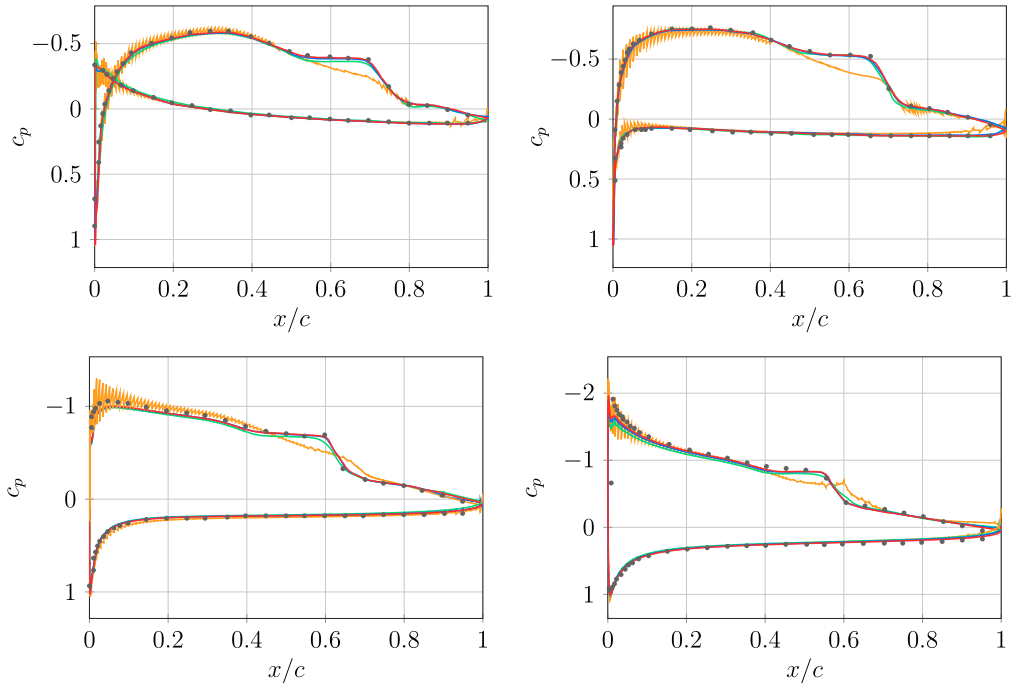

Fig. 29. Eppler E387 Airfoil. Pressure coefficient c_p distribution on the airfoil at different angles of attack, from 0° (top, right) to 6° (bottom, left), with the $\gamma k - \tilde{\omega}$ model, from $\mathbb{P}^1$ to $\mathbb{P}^4$ solution approximation. — $DG - \mathbb{P}^1$, — $DG - \mathbb{P}^2$, — $DG - \mathbb{P}^3$, — $DG - \mathbb{P}^4$, — Cakmakcioglu et al. SA-BCM model, • McGhee exp.

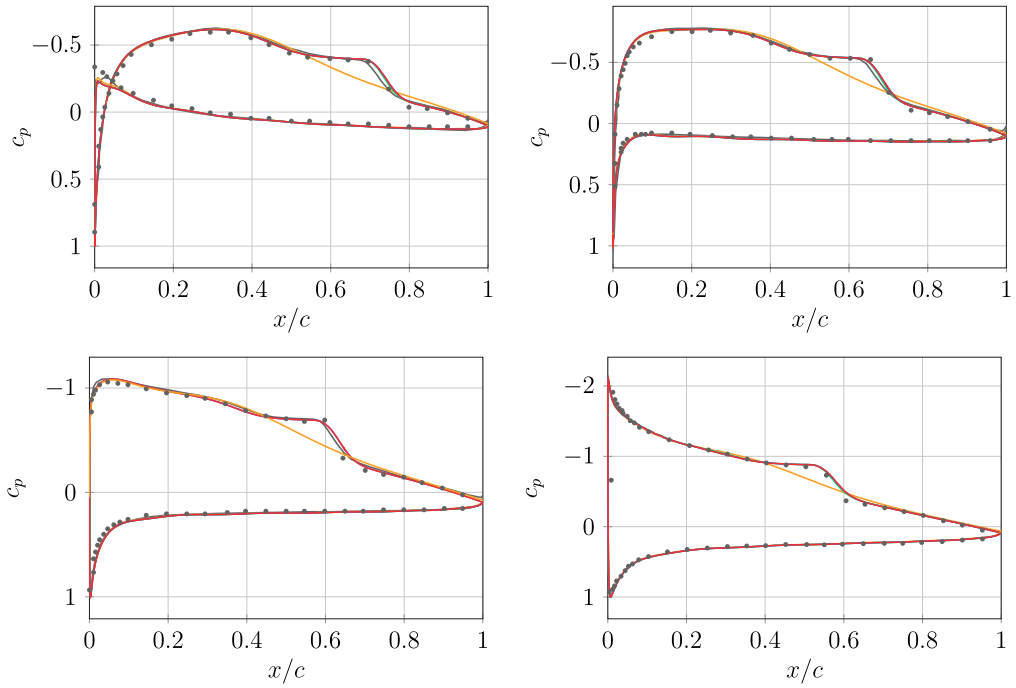

Fig. 30. Eppler E387 Airfoil. Pressure coefficient c_p distribution on the airfoil at different angles of attack, from 0° (top, right) to 6° (bottom, left), with the SA-BCM model and different freestream working variables $\tilde{\nu}_\infty$, $\mathbb{P}^4$ solution approximation. — $\tilde{\nu}_\infty/\nu = 1.5 \times 10^{0}$, — $\tilde{\nu}_\infty/\nu = 1.5 \times 10^{-1}$, — $\tilde{\nu}_\infty/\nu = 1.5 \times 10^{-2}$, — $\tilde{\nu}_\infty/\nu = 1.5 \times 10^{-3}$, — Cakmakcioglu et al. SA-BCM model, • McGhee exp.

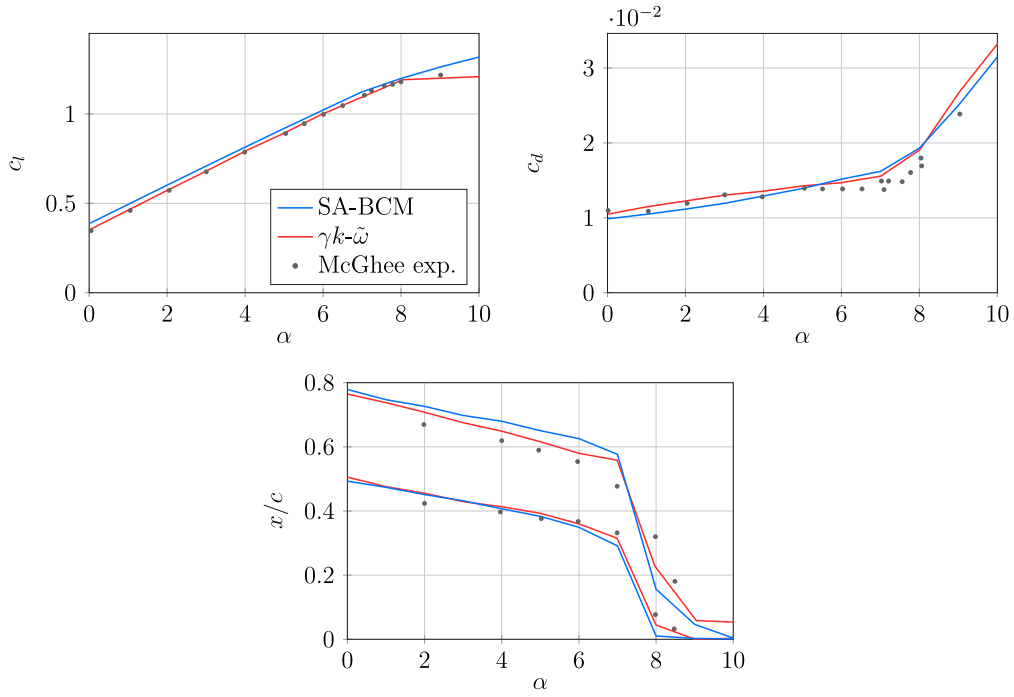

Fig. 31. Eppler E387 Airfoil. Lift c_l and drag c_d coefficient and the laminar separation (LS) and turbulent reattachment (TR) location with the $\gamma k - \tilde{\omega}$ and the SA-BCM model, $\mathbb{P}^4$ solution approximation.

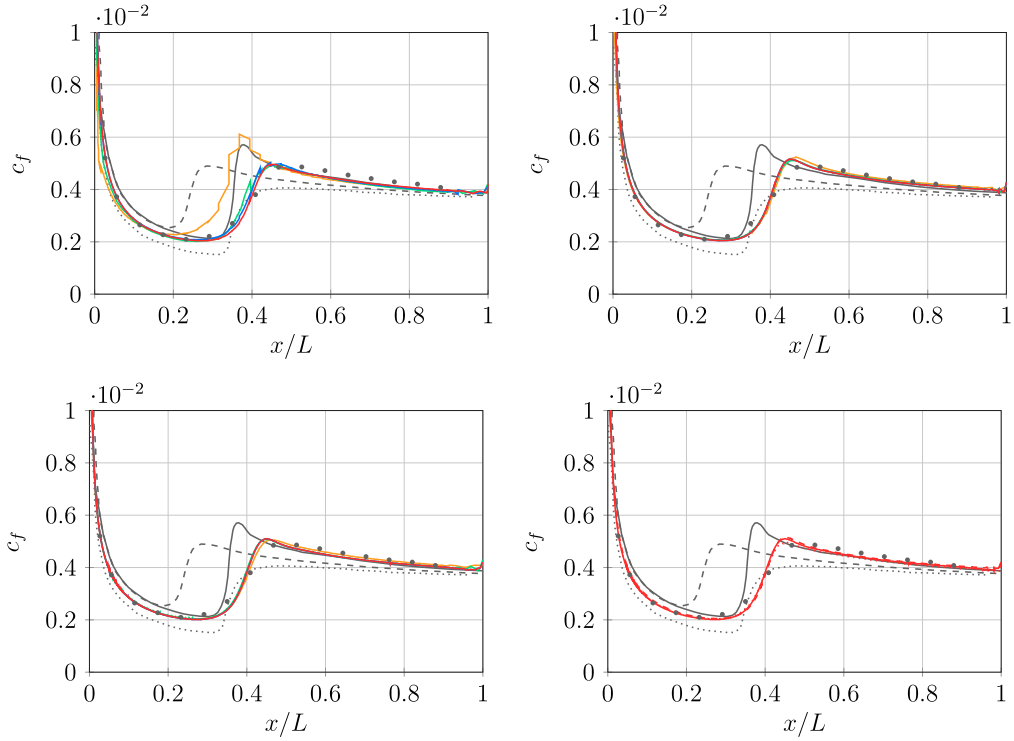

Fig. A.32. Zero pressure gradient flat plates. Skin friction coefficient c_f along the plate for the zero pressure gradient T3A flat plate with the $\gamma k - \tilde{\omega}$ model and different meshes: coarse (top, left), medium (top, right), and fine (bottom, left) and $\mathbb{P}^1$ to $\mathbb{P}^4$ solution approximation, and $\mathbb{P}^4$ solution approximation on the different meshes (bottom, right): coarse (dotted line), medium (dashed line) and fine (solid line) mesh. $DG - \mathbb{P}^1$, $DG - \mathbb{P}^2$, $DG - \mathbb{P}^3$, $DG - \mathbb{P}^4$, Holman and Fürst $\gamma k - \omega$ model, Cakmakcioglu et al. SA-BCM model, Kubacki et al. $\gamma k - \omega$ model, • Coupland exp.

Figs. A.32 and A.33 show the skin friction coefficient distributions on the T3A plate with the $\gamma k - \tilde{\omega}$ model and the SA-BCM model, with the different meshes and solution approximations, respectively. For the SA-BCM model the solutions are reported with the best values of the freestream working variables, e.g., $\tilde{\nu}_\infty/\nu = 1.5 \times 10^{-2}$. Figs. A.32 and A.33 show also the comparison of the $DG - \mathbb{P}^4$ solution approximation on the different meshes, in order to prove the convergence of the results increasing the order of the solution approximation as well as the number of elements of the mesh. The skin friction coefficients are almost overlapped and are in agreement with the experiments from

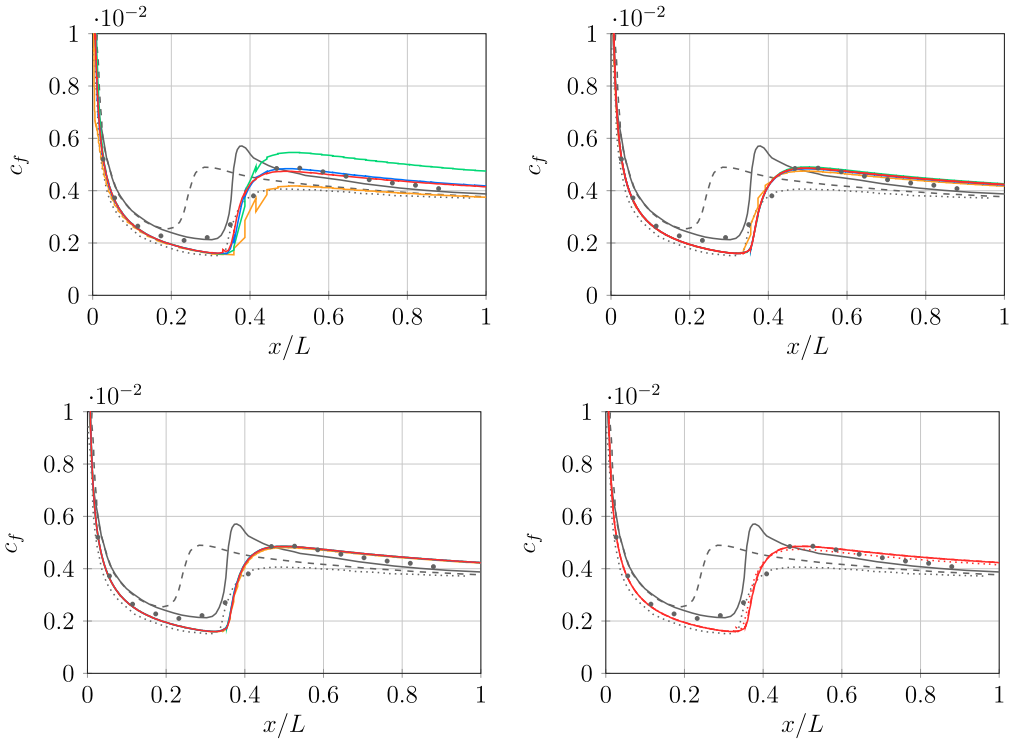

Fig. A.33. Zero pressure gradient flat plates. Skin friction coefficient c_f along the plate for the zero pressure gradient T3A flat plate with the SA-BCM model and different meshes: coarse (top, left), medium (top, right), and fine (bottom, left) and $\mathbb{P}^1$ to $\mathbb{P}^4$ solution approximation, and $\mathbb{P}^4$ solution approximation on the different meshes (bottom, right): coarse (dotted line), medium (dashed line) and fine (solid line) mesh. The solutions are here reported with the best values of the freestream working variables, e.g., $\tilde{\nu}_\infty/\nu = 1.5 \times 10^{-2}$. — $DG - \mathbb{P}^1$, — $DG - \mathbb{P}^2$, — $DG - \mathbb{P}^3$, — $DG - \mathbb{P}^4$, —— Holman and Fürst $\gamma k - \omega$ model, ····· Cakmakcioglu et al. SA-BCM model, – – – Kubacki et al. $\gamma k - \omega$ model, • Coupland exp.

Table A.6
Zero pressure gradient flat plates. Mesh details (top) and degrees of freedom (bottom) of the spatial sensitivity analysis. n_e is the number of elements, n_x is the number of element in x-direction on the wall, i.e., $x > 0$, n_y is the number of element in y-direction, and $\Delta y_1/L$ and $\Delta x_1/L$ are the height and length of the first element from the wall and from the leading edge of the plate in x-direction, respectively.

	Coarse mesh	Medium mesh	Fine mesh
n_e	2400	8800	33 600
$\Delta y_1/L = \Delta x_1/L$	0.0004	0.0002	0.0001
n_x	50	100	200
n_y	40	80	160
$DG - \mathbb{P}^1$	7200	26 400	100 800
$DG - \mathbb{P}^2$	14 400	52 800	201 600
$DG - \mathbb{P}^3$	24 000	88 000	336 000
$DG - \mathbb{P}^4$	36 000	132 000	504 000

$DG - \mathbb{P}^2$ solution approximation on the coarse and medium meshes, while with the fine mesh also the $DG - \mathbb{P}^1$ solution approximation is overlapped with the higher order solutions.

References

[1] Noventa G, Massa F, Bassi F, Colombo A, Franchina N, Ghidoni A. A high-order discontinuous Galerkin solver for unsteady incompressible turbulent flows. Comput & Fluids 2016;139:248–60. http://dx.doi.org/10.1016/j.compfluid.2016.03.007.

[2] Massa F, Noventa G, Lorini M, Bassi F, Ghidoni A. High-order linearly implicit two-step peer schemes for the discontinuous Galerkin solution of the incompressible Navier–Stokes equations. Comput & Fluids 2018;162:55–71. http://dx.doi.org/10.1016/j.compfluid.2017.12.003.

[3] Colombo A, Ghidoni A, Noventa G, Rebay S. p-Multigrid high-order discontinuous Galerkin solution of compressible flows. CISM Int Centre Mech Sci Courses Lect 2021;602:197–238.

[4] Crivellini A, D'Alessandro V, Bassi F. A spalart–Allmaras turbulence model implementation in a discontinuous Galerkin solver for incompressible flows. J Comput Phys 2013;241:388–415. http://dx.doi.org/10.1016/j.jcp.2012.12.038.

[5] Langtry RB, Menter FR, Likki SR, Suzen YB, Huang PG, Völker S. A correlation-based transition model using local variables - part II: Test cases and industrial applications. J Turbomach 2004;128(3):423–34. http://dx.doi.org/10.1115/1.2184353.

[6] Walters DK, Leylek JH. A new model for boundary layer transition using a single-point RANS approach. J Turbomach 2004;126(1):193–202. http://dx.doi.org/10.1115/1.1622709.

[7] Bassi F, Botti L, Colombo A, Crivellini A, De Bartolo C, Franchina N, Ghidoni A, Rebay S. Time integration in the discontinuous Galerkin code MIGALE - steady problems. In: Kroll N, Hirsch C, Bassi F, Johnston C, Hillewaert K, editors. IDIHOM: Industrialization of high-order methods - a top-down approach. Notes on Numerical Fluid Mechanics and Multidisciplinary Design, vol. 128, Cham: Springer International Publishing; 2015, p. 179–204.

[8] Holman J. Coupling the algebraic model of bypass transition with EARSM model of turbulence. Adv Comput Math 2019;45. http://dx.doi.org/10.1007/s10444-019-09680-2.

[9] Holman J, Fürst J. Numerical simulation of separation induced laminar to turbulent transition over an airfoil. J Comput Appl Math 2021;394:113530. http://dx.doi.org/10.1016/j.cam.2021.113530.

[10] Kubacki S, Dick E. An algebraic model for bypass transition in turbomachinery boundary layer flows. Int J Heat Fluid Flow 2016;58:68–83. http://dx.doi.org/10.1016/j.ijheatfluidflow.2016.01.001.

[11] Kubacki S, Dick E. An algebraic intermittency model for bypass, separation-induced and wake-induced transition. Int J Heat Fluid Flow 2016;62:344–61. http://dx.doi.org/10.1016/j.ijheatfluidflow.2016.09.013.

[12] Kubacki S, Simoni D, Lengani D, Dellacasagrande M, Dick E. Extension of an algebraic intermittency model for better prediction of transition in separated layers under strong free-stream turbulence. Int J Heat Fluid Flow 2021;92:108860. http://dx.doi.org/10.1016/j.ijheatfluidflow.2021.108860.

[13] Cakmakcioglu S, Bas O, Mura R, Kaynak U. A revised one-equation transitional model for external aerodynamics. In: AIAA aviation 2020 forum. 2020, http://dx.doi.org/10.2514/6.2020-2706, Chapter Applied CFD Modeling and Numerical Corrections with Experimental Data I.

[14] Mura R, Cakmakcioglu SC. A revised one-equation transitional model for external aerodynamics - part I: Theory, validation and base cases. In: AIAA aviation 2020 forum. 2020, http://dx.doi.org/10.2514/6.2020-2714, Chapter Applied CFD Modeling and Numerical Corrections with Experimental Data I.

[15] Bassi F, Colombo A, Crivellini A, Fidkowski KJ, Franciolini M, Ghidoni A, Noventa G. Entropy-adjoint p-adaptive discontinuous Galerkin method for the under-resolved simulation of turbulent flows. AIAA J 2020;58(9):3963–77. http://dx.doi.org/10.2514/1.J058847.

[16] Bassi F, Colombo A, Crivellini A, Fidkowski KJ, Franciolini M, Ghidoni A, Noventa G. An entropy-adjoint p-adaptive discontinuous Galerkin method for the under-resolved simulation of turbulent flows. 2019, p. 1–17. http://dx.doi.org/10.2514/6.2019-3418.

[17] Lorini M, Bassi F, Colombo A, Ghidoni A. High-order implementation of a non-local transition model in a DG solver for turbomachinery applications. Comput Fluids 2016;127:115–30. http://dx.doi.org/10.1016/j.compfluid.2020.104767.

[18] Coupland J. ERCOFTAC special interest group on laminar to turbulent transition and retransition: T3A and T3B test cases. Technical report, 1990.

[19] Coupland J, Brierley D. Transition in turbomachinery flows. BRITE/EURAM Project AERO-CT92-0050, 1996, Measurements available at the ERCOFTAC site.

[20] Mcghee RJ, Walker BS, Millard BF. Experimental results for the eppler 387 airfoil at low reynolds numbers in the langley low-turbulence pressure tunnel. Tech. rep., NASA Technical Memorandum 4062; 1988.

[21] Spalart PR, Garbaruk AV. Correction to the Spalart–Allmaras turbulence model, providing more accurate skin friction. AIAA J 2020;58(5):1903–5. http://dx.doi.org/10.2514/1.J059489, arXiv:https://doi.org/10.2514/1.J059489.

[22] Ilinca F, Pelletier D. Positivity preservation and adaptive solution for the k-? Model of turbulence. AIAA J 1998;36(1):44–50. http://dx.doi.org/10.2514/2.350, arXiv:https://doi.org/10.2514/2.350.

[23] Bassi F, Crivellini A, Rebay S, Savini M. Discontinuous Galerkin solution of the Reynolds-averaged Navier-Stokes and k-ω turbulence model equations. Comput & Fluids 2005;34:507–40.

[24] Bassi F, Botti L, Colombo A, Crivellini A, Franchina N, Ghidoni A, Rebay S. Very high-order accurate discontinuous Galerkin computation of transonic turbulent flows on aeronautical configurations. In: Kroll N, Bieler H, Deconinck H, Couaillier V, Ven H, Sorensen K, editors. ADIGMA - a european initiative on the development of adaptive higher-order variational methods for aerospace applications. Notes on Numerical Fluid Mechanics and Multidisciplinary Design, vol. 113, Springer Berlin Heidelberg; 2010, p. 25–38. http://dx.doi.org/10.1007/978-3-642-03707-8_3.

[25] Bassi F, Botti L, Colombo A, Crivellini A, Ghidoni A, Nigro A, Rebay S. Time integration in the discontinuous Galerkin code MIGALE - unsteady problems. In: Kroll N, Hirsch C, Bassi F, Johnston C, Hillewaert K, editors. IDIHOM: Industrialization of high-order methods - a top-down approach. Notes on Numerical Fluid Mechanics and Multidisciplinary Design, vol. 128, Springer International Publishing; 2015, p. 205–30.

[26] Walters DK, Cokljat D. A three-equation Eddy-viscosity model for Reynolds-averaged Navier-Stokes simulations of transitional flow. J Fluids Eng 2008;130(12):1–14. http://dx.doi.org/10.1115/1.2979230.

[27] Lorini M, Bassi F, Colombo A, Ghidoni A, Noventa G. Discontinuous Galerkin solution of the RANS and k_L-k-$\tilde{\omega}$ equations for natural and bypass transition. Comput & Fluids 2021;214:104767. http://dx.doi.org/10.1016/j.compfluid.2020.104767.

[28] Bassi A, Colombo A, Ghidoni A, Lorini M, Noventa G. Discontinuous Galerkin solution of the Reynolds-averaged Navier-Stokes and k_L-k-$\tilde{\omega}$ transition model equations. In: ECCOMAS congress 2016 - proceedings of the 7th european congress on computational methods in applied sciences and engineering, Vol. 2. 2016, p. 2632–47. http://dx.doi.org/10.7712/100016.1986.6971.

[29] Shih T-H, Liou WW, Shabbir A, Yang Z, Zhu J. A new k-ε eddy viscosity model for high reynolds number turbulent flows. Comput & Fluids 1995;24(3):227–38.

[30] Zaki TA, Wissink JG, Rodi W, Durbin PA. Direct numerical simulations of transition in a compressor cascade: the influence of free-stream turbulence. J Fluid Mech 2010;665:57–98. http://dx.doi.org/10.1017/S0022112010003873.

[31] Kubacki S, Gorecki B, Dick E. Extension of an algebraic intermittency model for better prediction of transition in separated layers under strong free-stream turbulence. In: 11^{Th} european conference on turbomachinery fluid dynamics and thermodynamics, european turbomachinery society.

[32] Noventa G, Massa F, Rebay S, Bassi F, Ghidoni A. Robustness and efficiency of an implicit time-adaptive discontinuous Galerkin solver for unsteady flows. Comput & Fluids 2020;204. http://dx.doi.org/10.1016/j.compfluid.2020.104529.

[33] Gottlieb J, Groth C. Assessment of Riemann solvers for unsteady one-dimensional inviscid flows of perfect gases. J Comput Phys 1988;78(2):437–58.

[34] Balay S, Buschelman K, Gropp WD, Kaushik D, Knepley MG, McInnes LC, Smith BF, Zhang H. PETSc web page. 2001, http://www.mcs.anl.gov/petsc.

[35] Bassi F, Botti L, Colombo A, Pietro DD, Tesini P. On the flexibility of agglomeration based physical space discontinuous Galerkin discretizations. J Comput Phys 2012;231(1):45–65.

[36] Vlahostergios Z, Yakinthos K, Goulas A. Separation-induced boundary layer transition: Modeling with a non-linear eddy-viscosity model coupled with the laminar kinetic energy equation. Int J Heat Fluid Flow 2009;30:617–36. http://dx.doi.org/10.1016/j.ijheatfluidflow.2009.02.004.

[37] Bassi F, Botti L, Colombo A, Crivellini A, Franciolini M, Ghidoni A, Noventa G. A p-adaptive matrix-free discontinuous Galerkin method for the implicit LES of incompressible transitional flows. Flow Turbul Combust 2020;105(2):437–70. http://dx.doi.org/10.1007/s10494-020-00178-2.

[38] Evans R. Some turbulence and unsteadiness ef fects in turbomachinery. Turbul Intern Flows 1976;10(3):485–516.

[39] Holland R, Evans R. The effects of periodic wake structures on turbulent boundary layers. J Fluids Struct 1996;10(3):269–80. http://dx.doi.org/10.1006/jfls.1996.0016.

[40] Menter FR, Matyushenko A, Lechner R, Stabnikov A, Garbaruk A. An algebraic LCTM model for laminar-turbulent transition prediction. Flow Turbul Combust 2022. http://dx.doi.org/10.1007/s10494-022-00336-8.